Corrosion and Passivation of Mg-Al and Ni-Cr Alloys

by

Ashlee Aiello

A Dissertation Presented in Partial Fulfillment
of the Requirements for the Degree
Doctor of Philosophy

Approved July 2018 by the
Graduate Supervisory Committee:

Karl Sieradzki, Chair
Daniel Buttry
Candace Chan
Peter Crozier

ARIZONA STATE UNIVERSITY

December 2018

ABSTRACT

In this dissertation, micro-galvanic corrosion effects and passivation behavior of single-phase binary alloys have been studied in order to formulate new insights towards the development of “stainless-like” lightweight alloys. As a lightweight material of interest, Mg-xAl alloys were studied using aqueous free corrosion, atmospheric corrosion, dissolution rate kinetics, and ionic liquid dissolution. Polarization and “accelerated” free corrosion studies in aqueous chloride were used to characterize the corrosion behavior and morphology of alloys. Atmospheric corrosion experiments revealed surface roughness and pH evolution behavior in aqueous environment. Dissolution in absence of water using choline-chloride:urea ionic liquid allowed for a simpler dissolution mechanism to be observed, providing additional insights regarding surface mobility of Al. These results were compared with commercial alloy (AZ31B, AM60, and AZ91D) behavior to better elucidate effects associated with secondary phases and intermetallic particles often present in Mg alloys. Aqueous free corrosion, “accelerated” free corrosion and ionic liquid dissolution studies have confirmed Al surface enrichment in a variety of morphologies, including Al-rich platelet and Al nanowire formation. This behavior is attributed to the preferential dissolution of Al as the more “noble” element in the matrix. Inductively-coupled mass spectroscopy was used to measure first-order rate reaction constants for elemental Mg and Al dissolution in aqueous chloride environment to be $k_{Mg} = 9.419 \times 10^{-6}$ and $k_{Al} = 2.103 \times 10^{-6}$ for future implementation in kinetic Monte Carlo simulations. To better understand how “stainless-like” passivation may be

achieved, Ni-xCr alloys were studied using polarization and potential pulse experiments. The passivation potential, critical current density, and passivation current density were found to decay with increasing Cr composition. The measured average number of monolayers dissolved during passivation was found to be in good agreement with percolation theory, with a fitted 3-D percolation threshold of $p_c^{3D} = 0.118$ compared with the theoretical value of 0.137. Using these results, possible approaches towards achieving passivation in other systems, including Mg-Al, are discussed.

In dedication to my loving husband. I would be lost without you. Only you could fill my darkest moments with light.

ACKNOWLEDGMENTS

I would like to express the utmost gratitude and thankfulness for my advisor Karl. Prior to meeting Karl, a doctoral degree had never been a consideration, let alone a possibility to me. He has always been so generous with his vast reservoir of knowledge, and I have grown so much during my time with him. I cannot thank him enough for the endless patience, kindness, and understanding he has shown me. This has truly been a life changing experience for me in so many ways.

I would also like to thank my committee members Prof. Daniel Buttry, Prof. Candace Chan, and Prof. Peter Crozier for their willingness to participate in my research. Each of you has offered valuable and unique insights and advice. I would like to thank Dr. Allison Handler, Dr. Qing Chen, Julia Fisher, and Anna Weiss for their contributions towards the development of the magnesium program.

I thank my mentors and group members—Dr. Allison Handler, Erin Karasz, Ke Geng, and Julia Fisher—for their support and many thoughtful discussions, especially when I have felt lost along my way. I am so thankful this journey has brought you all into my life.

Most of all, I thank my husband Ken. I never imagined that choosing to pursue my PhD would also mean meeting the love of my life. I thank God every day for you.

Special thanks goes to the Department of Energy Office of Energy Efficiency and Renewable Energy, Lightweight Materials, Vehicle Technology Office (*Contract No: DE-EE0006436*) for support on Mg alloy corrosion and the National Science Foundation Division of Materials Research (*Contract No: 1708459*) for support of Ni-Cr alloy investigations.

TABLE OF CONTENTS

Page

CHAPTER Page

CHAPTER Page

LIST OF TABLES

Table Page

LIST OF FIGURES

FIGURE Page

FIGURE Page

FIGURE Page

FIGURE Page

1 Introduction

Magnesium has become a popular source of commercial interest for lightweight structural applications. In addition to its low density of 1.738 g/cm^3, magnesium possesses several other desirable industrial attributes—it is the eighth most abundant resource in the world, has a high strength-to-weight ratio, and can be easily processed using casting methods [1]–[6]. Magnesium is also an ideal component for biological applications; it plays an essential role in many physiological functions in the human body with a consumption rate of ~250-500 mg day^{-1} [4]. In fact, approximately 20 g of magnesium is present in the human body at all times, and a toxic dosage has yet to be identified [4]. This combination of properties is particularly desirable for the transportation, aerospace, and biomedical industries.

Although there are several commercially available magnesium alloys (e.g. AZ31B, AM60 and AZ91D), the primary obstacle for consistent industrial implementation of magnesium is its high susceptibility to corrosion. As shown in Table 1.1, magnesium is highly electrochemically reactive with a low standard potential of -2.370 V vs. SHE. Magnesium does not form a passive film under atmospheric conditions, leaving it susceptible to corrosion attackers and internal galvanic corrosion [7]. This material is also difficult to alloy since it has a strong tendency towards formation of secondary phases, leading to increased microgalvanic corrosion [8]. The magnesium dissolution process is rather complicated, as it is governed by a combination of four simultaneous

electrochemical and chemical reactions involving magnesium dissolution, oxide formation, and oxide hydration [9]. While these reactions are agreed upon within the scientific community, the dissolution behavior at the surface, including microgalvanic effects on alloying, are not well understood.

Single phase alloy systems are the simplest to observe electrochemically since the presence of multiple phases introduces a galvanic coupling effect with numerous complications to consider. Aluminum is known for atmospheric formation of a passive film and exhibits one of the highest solubilities in solid-solution with magnesium. In an effort to elucidate some of the surface mechanisms occurring during active dissolution of magnesium alloys, primarily regarding compositional changes and secondary phase formation, we have studied Mg-xAl single-phase alloys using aqueous free corrosion, atmospheric corrosion, reaction rate kinetics, and ionic liquid dissolution.

While “noble” element enrichment was consistently observed during these studies, passivation was never achieved. To further explore passivation mechanisms in solid-solution alloys, the Ni-Cr system was studied. Stainless steels are well known for their passive behavior in atmospheric conditions with additions of approximately 12-13 at.% Cr. Although this fact is regularly implemented in industrial applications, passive film formation in stainless steels is not well understood. The Ni-Cr and Fe-Cr systems display similar passive behavior with additions of 12-13 at.% Cr. Referencing the electromotive force series in Table 1.1., nickel is less electrochemically active than iron and forms only

one oxidation state as opposed to two. Additionally, the packing order of the close packed planes in FCC (i.e. Ni-Cr alloys) and HCP (i.e. Mg) crystals are more closely related than BCC (i.e. Fe-Cr) and HCP crystals. As such, we have chosen the Ni-Cr system as our "ideal" example of a passive solid-solution alloy. Unfortunately, the dissolution behavior of Ni-Cr alloys has not been electrochemically well studied and only a few reports exist in the literature [10]–[12]. To gain a better understanding of passivation behavior in single-phase alloys, polarization and potential pulse studies were used in Ni-xCr alloys. By connecting these results to percolation theory, we have been able to further our understanding of passive film formation in single-phase alloys and formulate new ideas regarding the development of "stainless-like" magnesium alloys.

Electromotive force series	
Electrode reaction	Standard Potential, E^0 (V VS. SHE)
$Au^{3+} + 3e^- \rightarrow Au$	1.500
$Pt^{2+} + 2e^- \rightarrow Pt$	1.200
$Hg^{2+} + 2e^- \rightarrow Hg$	0.854
$Ag^{+} + e^- \rightarrow Ag$	0.800
$Cu^{+} + e^- \rightarrow Cu$	0.521
$Cu^{2+} + 2e^- \rightarrow Cu$	0.337
$2H^{+} + 2e^- \rightarrow H_2$	**0.000**
$Fe^{3+} + 3e^- \rightarrow Fe$	-0.036
$Ni^{2+} + 2e^- \rightarrow Ni$	-0.250
$Cd^{2+} + 2e^- \rightarrow Cd$	-0.403
$Fe^{2+} + 2e^- \rightarrow Fe$	–0.440
$Cr^{3+} + 3e^- \rightarrow Cr$	–0.740
$Zn^{2+} + 2e^- \rightarrow Zn$	–0.763
$Mn^{2+} + 2e^- \rightarrow Mn$	–1.180
$Zr^{4+} + 4e^- \rightarrow Zr$	–1.530
$Al^{3+} + 3e^- \rightarrow Al$	–1.660
$Mg^{2+} + 2e^- \rightarrow Mg$	–2.370
$Li^{2+} + 2e^- \rightarrow Li$	–3.050

Table 1.1. Electromotive force series for common metals [13].

2 Overview of Techniques and Methods

2.1 Electrochemical Methods

2.1.1 Electrochemical Cell Types

Two primary electrochemical cells were used, depending on the experiment type– (1) two electrode and (2) three electrode. As indicated by their name, two electrode cells are comprised of two components suspended in conductive electrolyte—(1) working electrode and (2) reference electrode. The two electrode cell is an open circuit system where no outside current is passed through the system. The working electrode provides the site of the desired measurement while the reference electrode serves as the designated standard by which potentials are measured by the potentiostat. In a two electrode system, the potential at zero current, or the open circuit potential (OCP), can be monitored using a potentiostat.

Three electrode cells are closed systems requiring three primary components—(1) working electrode, (2) reference electrode, and (3) counter electrode. Just as with the two electrode cell, the working electrode serves as the measurement site, and the reference electrode sets the standard by which potentials are measured. In order to measure and control the current of the system, however, a counter electrode is required. For any external charge maintained at the working electrode, an equal and opposite charge must

be maintained at the counter electrode. By applying a known potential or current, reactions can be observed and controlled. The counter electrode is composed of inert material to prevent electrochemical reactions from taking place at the surface. In the case of metallic corrosion studies, the working electrode typically serves as the anode, where oxidation occurs, and the counter electrode serves as the cathode, where reduction occurs. In all experiments performed, platinum serves as the counter electrode in either bulk or mesh form. It is important that the counter electrode surface area should be greater than that of the working electrode to prevent kinetic limitations.

Electrochemical studies rely on system responses to an applied current or potential to understand electrochemical systems. Current and potential measurements are typically recorded using a potentiostat, which controls the potential difference between the working and reference electrodes. A Gamry Interface 1000E potentiostat was used to perform all electrochemical experiments.

2.1.2 Potentiostatic Experiments

Five primary potentiostatic experiment formats were used for electrochemical studies. These include: (1) open circuit potential or corrosion potential measurements (OCP), (2) chronoamperometry (CA), (3) chronocoloumetry, (4) linear sweep voltammetry (LSV), and (5) cyclic voltammetry (CV). For open circuit and/or corrosion potential monitoring,

a two electrode system is used, and the open circuit potential is simply monitored for a specified duration by taking OCP measurements every specified number of seconds. The remaining four potentiostatic experiments require a three electrode setup since they rely on either an applied potential or current. Chronoamperometry measures the current as a function of time while a specified potential is applied to the system. These experiments typically run for either specified duration or until a specified current limit is reached. Similarly, chronocoulometry measures the charge that has been passed as a function of time while a specified potential is applied to the system. The potentiostat will continuously calculate the integrated area beneath the current vs. time curve to measure the passed charge. Just as with chronoamperometry, these experiments can run for either specified duration or until a specified charge limit has been reached. Chronocoulometry is especially useful when electrodepositing a layer of specified thickness. Linear sweep voltammetry is a more dynamic experiment, where the current is measured within a user-defined potential window. Controlled parameters include the potential step size, scan rate, and current limit. A common use of linear sweep voltammetry in corrosion experiments is for observation of the polarization behavior of the corrosion reaction to observe reaction kinetics and corrosion potential. Cyclic voltammetry is similar to LSV in the sense that the current is measured within a specified potential window. A CV does not stop after one sweep in a specified direction, however. Instead, it will stop at the potential limit and begin scanning in the opposite direction until the next potential limit is reached. In addition to the step size, sweep rate, and current limit, the scan direction and number of cycles can be specified by the user.

2.2 Microscopy

The majority of surface analysis of samples was performed using scanning electron microscopy (SEM) and energy-dispersive x-ray spectroscopy (EDS). This combination of techniques can be used to provide high magnification surface imaging and compositional data, and they can be performed simultaneously when an X-ray detector is fitted onto the SEM. A simplified diagram of an SEM with fitted X-ray detector is provided in Figure 2.1. The entire column is maintained under vacuum, requiring a separate chamber for insertion and removal of the sample. An electron beam source is heated to thermoionically produce an electron beam (e-beam), which is directed towards the sample surface using condenser and aperture lenses. When the e-beam hits the sample surface, the beam electrons will interact with electrons in the sample atoms, resulting in electron scattering, producing secondary electrons, backscattered electrons, and x-ray emissions. These signals are collected as the beam is scanned along the sample surface for imaging and compositional purposes. SEM imaging and EDS compositional data was collected using a Philips XL30 SEM.

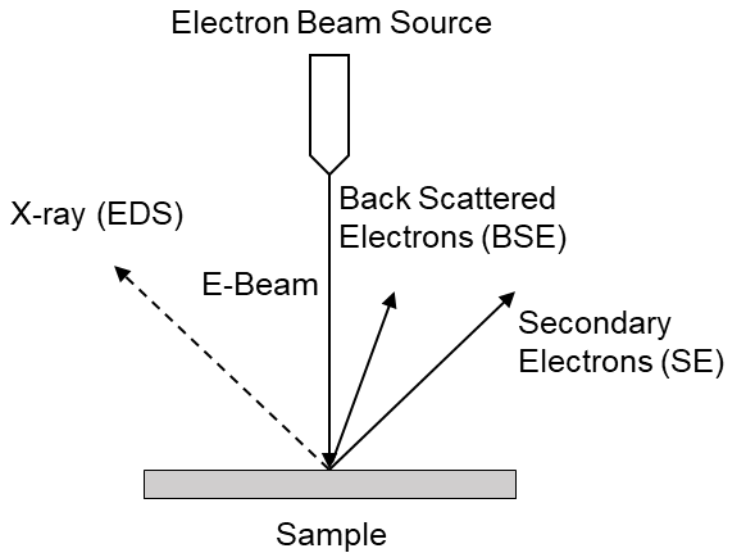

Figure 2.1. Diagram of SEM and EDS.

For SEM imaging, secondary electrons (SE) or backscattered electrons (BSE) can be used as the image source. Low-energy secondary electrons are produced by inelastic scattering, meaning that the kinetic energy of the incident electron is not conserved. Secondary electrons are produced from the outer electron shells and are characterized by energies of 50 eV or less. Secondary electrons are used for high-resolution imaging, as this is a more surface sensitive technique. Backscattered electrons, meanwhile, are produced by elastic scattering where the kinetic energy of the incident electron is conserved. Backscattered electrons are sourced from the lower electron shells at the atomic nuclei. The strength of the backscattered electron signal is dependent on the atomic number of the source atom with the strength increasing as the atomic number grows higher. BSE imaging is particularly useful for providing contrast between different phases or materials.

Energy-dispersive x-ray spectroscopy (EDS) relies on x-ray photon emissions as the electron beam interacts with the sample surface. When core electrons are ejected from sample atoms, the atom enters an excited state. To return to a neutral state, an x-ray photon is emitted. The energy of the photon is dependent on the atomic number of the atom, allowing for compositional data to be obtained. EDS can be used to obtain compositions of the overall image area, specified areas, or for elemental mapping.

3 Magnesium-Aluminum

3.1. Introduction

3.1.1. Magnesium as a material of interest

Magnesium has become a highly desirable metal, particularly for the aerospace, automotive, and biomedical industries, due to its high abundancy, high strength-to-weight ratio, good castability, biocompatibility, and high thermal conductivity [1]–[6]. Unfortunately, magnesium displays poor corrosion-resistance and is highly reactive in the presence of corrosion attackers, susceptible to internal galvanic corrosion, and unable to form a stable passive film. While magnesium does form a quasi-passive film of $Mg(OH)_2$ in aqueous environment, this film is only stable at pH levels greater than 11 [9], is vulnerable to corrosion attackers, and demonstrates poor pitting resistance [7]. Strong passive films perform three key functions—(1) restriction of outward flow of cations, (2) resistance of inward flow of damaging anions or oxidants, and (3) rapid repair of localized damage [7]. In metals, these passive layers are often characterized as a thin, oxidized, protective film in the presence of corrosive aqueous environments [14].

3.1.2. Magnesium coatings

Common ways to increase the corrosion resistance of metals include the use of a protective coating or alloying agent. Protective coatings are often not of interest, however, unless they possess self-healing properties. While intact, coatings can provide an effective electrochemical barrier between the metal and a corrosive environment (e.g. seawater). In the event that a coating is damaged, by a scratch for instance, galvanic corrosion will ensue with the coating acting as the cathode and the now exposed area acting as the anode. Due to the small exposed area of the anode in comparison with the cathodic area, the coated material experiences rapid localized attack. This corrosion mechanism means that any small defect in the coating can cause catastrophic damage to the coated material, although this can be eliminated were the coating capable of self-healing (i.e. metal oxide formation). One of the most common and successful coatings used for corrosion-susceptible alloys, including Mg, are chromate convergent coatings. Due to the high toxicity and carcinogenic nature of chromate convergent coatings, however, they have been gradually removed from use despite the lack of a reliable replacement. The low reversible metal/metal-ion electrochemical potential of Mg eliminates nearly all metallic coating options. Recent work done by Hiromoto describes self-healing properties of hydroxyapatite and octacalcium phosphate coatings on both AZ31B and Mg during 4-6 week observation in 0.9% NaCl [15]. Hiromoto reports a two-layer self-healing mechanism, a Mg, P, and O based layer that forms initially at the exposed surface, followed by a Ca, P, and O outer layer. NEI Corporation has created

NANOMYTE PT-60, a chromate-free conversion coating that reportedly displays similar corrosion behavior to chromate conversion coatings on AZ91D substrate [16]. Data surrounding this is limited, however, as this is a patent-pending technology. Other forms of convergent coatings have been reported on Mg, although the lack of self-healing properties significantly reduces their application possibilities [17],[18]. The development for self-healing, chromate-free coatings remains an area of demand with continued interest.

3.1.3 Alloying magnesium

Alloying agents can be used to improve the corrosion performance of a material by altering the material properties. This can introduce a wide range of complications, however, since multiple material properties are influenced by addition of alloying agent(s), such as number of phases, grain size, crystal structure, ductility, density, etc. Solubility is an especially important factor to consider, especially in the case of highly reactive metals, since exceeding the solubility limit results in precipitation of secondary phases, introducing galvanic corrosion effects. Although the microgalvanic corrosion rates can be controlled by particle size, spacing, area fraction, and electrochemical properties (i.e. cathodic kinetics and open circuit potential), secondary phases are considered highly undesirable are a current issue with commercially available Mg-Al alloys (e.g. AZ31B, AM60, and AZ91D) [19]–[24].

For our purposes, the alloying agent should be able to form a passive film in atmospheric conditions, display solubility in solid solution with magnesium, and have a low enough density to maintain the desirable lightweight properties of the material. Figure 3.1. shows elemental solubility in solid solution and corresponding alloy density for binary alloys fully saturated with the secondary component. With the exception of Cd, no metals exhibit over 20 at.% solubility in solid solution with Mg. Magnesium displays a high tendency towards the formation of secondary-phase intermetallics at thermodynamic equilibrium that accumulate at the grain-boundary interface. Only six metallic elements display solubilities over 10 at.% in solid solution with Mg – Cd, In, Li, Tl, Sc, and Al. Of these, only Cd and Al display any corrosion resistance in atmospheric conditions. Cd, although it displays full solubility in solid solution with Mg, is toxic and has an extremely high density (8.7 g/cm^3) compared with Mg making it completely unsuitable for production of lightweight materials.

Recent reports of a newly developed Mg-33 at.% Li alloy, in combination with small quantities of Al, Y, and Zr, measure a corrosion potential approximately 225 mV more positive than that of pure Mg in 0.1M NaCl [25]. This result is somewhat unexpected, as Li is more electrochemically active than Mg and known for its high reactivity in aqueous conditions. The alloy also displays improved mechanical performance (higher specific strength, increased ductility, and higher yield strength) compared with pure Mg and commercially available Mg alloys. Limited testing of these alloys in atmospheric conditions has been performed, however, as imaging of the sample is only available for 1

hour immersion in 0.01M NaCl [26]. Previous corrosion studies by Makar et. al. of binary-phase Mg-Li (up to 14% Li) alloys report decreased corrosion performance compared with pure Mg [27]. Additionally, the high Li content of this alloy may pose an issue for commercial applications due to the already high demand placed by lubricant, battery, ceramic glass, and dye industries.

Al presents itself as the strong commercial candidate since it is corrosion-resistant, highly abundant, cost-effective, and displays low toxicity. As shown in the phase diagram provided in Figure 3.2, Al is soluble in solid solution with Mg up to just under 12 at.%. At higher concentrations, β-phase Mg will form, accompanied by a crystal structure shift (Table 3.1.). Studies of binary-phase Mg alloys performed by Makar et.al. using Al, Zn, Li, Ca, and Si revealed slower corrosion rates only for Al containing alloys, with the corrosion rate decreasing with increasing Al concentration [27].

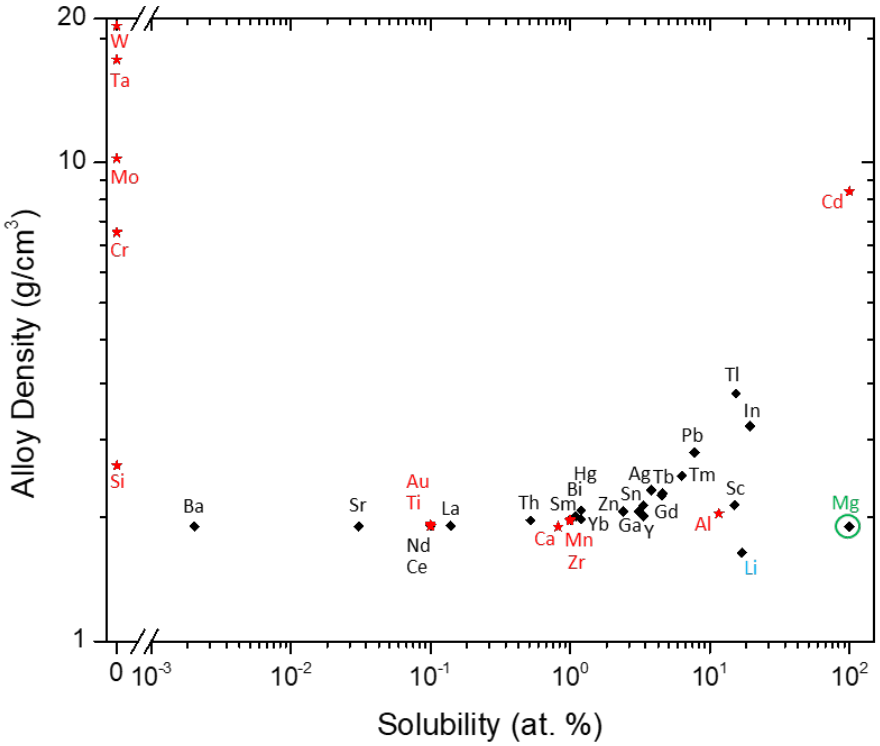

Figure 3.1. Alloy density as a function of solubility in solid solution with magnesium. Red data points mark elements with strong corrosion performance [8].

To gain a more complete understanding of the corrosion mechanism of magnesium, both as an elemental component and within the magnesium-aluminum binary system, four primary areas of interest have been identified: (1) aqueous free corrosion, (2) atmospheric corrosion, (3) dissolution rate kinetics, and (4) corrosion in absence of water. Aqueous free corrosion and atmospheric corrosion studies provide a baseline for the typical corrosion behavior of these materials. By studying the dissolution rate of Mg and Al, first-order rate kinetic expressions have been experimentally-derived. In an effort to study Mg-dissolution in absence of cathodic surface reactions that occur in aqueous environments, ionic dissolution studies were performed.

3.2. Background

3.2.1. Commercial Mg-Al Alloys and Processing Methods

Several commercial forms of Mg-Al alloys are available, including AZ31B, AM60, and AZ91D, which contain approximately 3, 6, and 9 wt.% Al, respectively. Additional alloying agents are used to influence grain size and corrosion resistance, and the full composition of these three alloys is provided in Table 3.2. As a result, all three alloys contain intermetallic particles and secondary phases. This morphology can typically be described via three primary phases: (1) α-phase (solid solution Al in Mg), (2) β-phase ($Mg_{17}Al_{12}$), and (3) intermetallic phases containing Mn, Fe, and Al [20],[28]. The corrosion performance of alloys containing multiple phases is highly dependent on grain size, area fraction of phases, and spatial distribution of phases and intermetallic particles. Multiple studies have shown that increases in the amount of solid solution result in lower corrosion rates [19],[20]. Bland et.al. have also gone on to report effects of intermetallic particle size and spacing [19]. Their results show that maintaining the same area fraction, but increasing the distance between intermetallic particles (creating larger particle size) also reduced corrosion rates and limited the majority of corrosion to the area at the intermetallic particle/Mg interface. Aung and Zhou have also reported the presence of twins and large grain size to increase corrosion rates in AZ31B alloys [23].

Various processing methods and alloying agents are often used to control the grain size, area fraction of phases, and spatial distribution of phases within the alloy. Most Mg alloys are formed using casting or forming methods [29]. Casting is the most common form of Mg alloy production, mainly high-pressure die-casting and gravity casting (i.e. sand and permanent mold casting), although squeeze casting, thixo-casting, and thixomolding are also used [29]. Most forming processes can be performed on Mg alloys at elevated temperature (230°C - 370°C), and wrought alloys typically display higher strength and ductility in comparison with cast alloys, although this is at the sacrifice of surface quality and corrosion performance [29]. The high reactivity of magnesium, combined with its less formable hcp structure (compared with the more ideal cubic structures) has always presented a challenge when creating magnesium alloys, although new techniques are constantly being investigated to improve processing methods. Recent work by Zander and Schnatterer, for instance, has shown improved corrosion resistance in thixomolded AZ91D when compared with twin-roll casting and high-pressure die casting due to its influence on microstructure uniformity [30]. Small amounts of various alloying agents can be used to control the grain size of alloys as well, including Ti, Zr, Si, Cu, Ag, Sn, Co, and Mn [3]. Small additions of Mn are popular for improved corrosion performance in Mg alloys due to a sheathing effect or formation of intermetallic phases with cathodic impurity particles such as Fe [31]. The use of Zn, meanwhile, targets mechanical property improvement since it provides greater strength benefits over Al although it can only be used at small concentrations owing to its high density and low solubility in α-Mg [32]–[34].

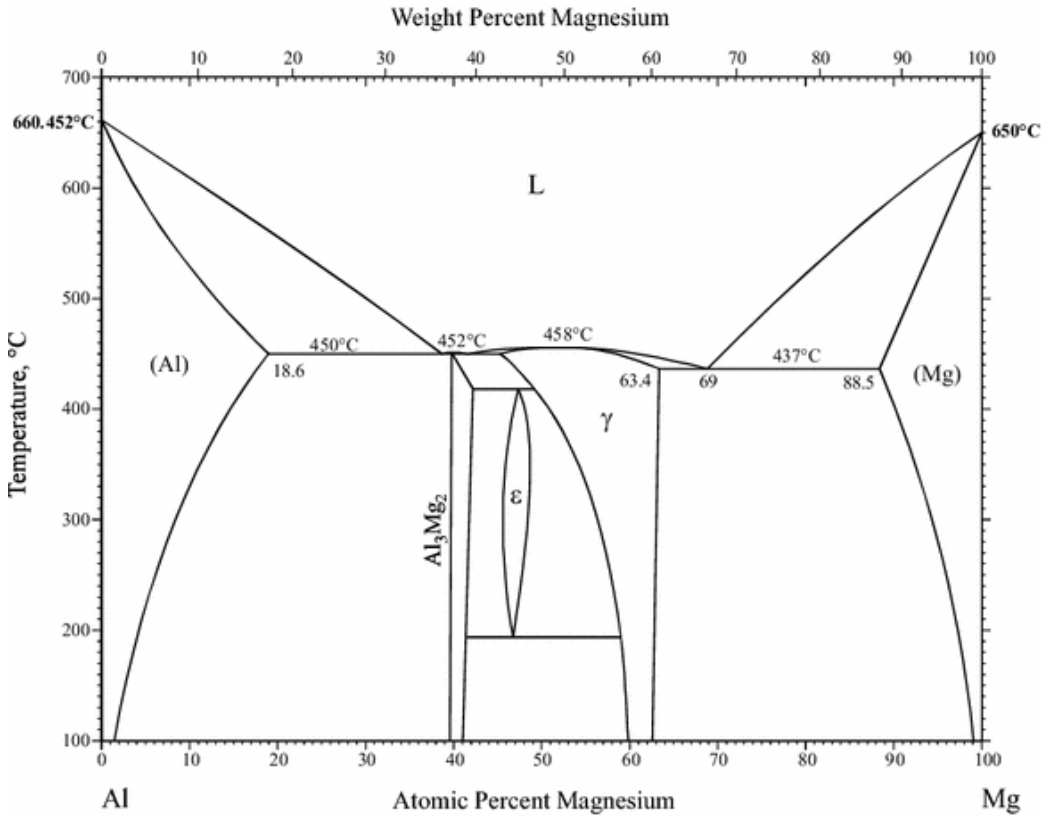

Figure 3.2. Al-Mg phase diagram [35].

Material	Structure	Point Group	Space Group	Lattice Parameters		
				a	b	c
Mg	HCP	6/mmm	$P6_3/mmc$	3.209	3.209	5.211
Al	FCC	m $\bar{3}$m	Fm $\bar{3}$m	4.046	4.046	4.046
Al_2O_3	Trigonal	$\bar{3}$m	R $\bar{3}$c	4.785	4.785	12.99
β-Mg	BCC	$\bar{4}$3m	I $\bar{4}$3m	10.56	10.56	10.56
$Mg(OH)_2$	PH	$\bar{3}$m	P $\bar{3}$m	3.120	3.120	4.730
MgO	FCC	m $\bar{3}$m	Fm $\bar{3}$m	4.212	4.212	4.212

Table 3.1. Relevant crystal structures of the Mg-Al system [8].

3.2.2. Dissolution Mechanism

Magnesium dissolution is governed by four primary reactions (Equations. 3.1-3.4) [9]. The reversible metal/metal-ion electrochemical potential of magnesium is -2.37 V (vs. NHE) (Equation 3.1), however the experimental OCP is measured at ~ -1.5 V (vs. NHE) in aqueous electrolyte due to the formation of the quasi-passive $Mg(OH)_2$ film. While the primary anodic reaction, dissolution of Mg, is described by Equation 3.1, Mg will simultaneously react with water via three mechanisms (Equations. 3.2-3.4) to produce various quasi-passive films. These include the formation of magnesium oxide (Equation. 3.2), hydration of magnesium oxide to produce a magnesium hydroxide (Equation. 3.3), and additional creation of magnesium oxide via hydration of magnesium anions (Equation. 3.4). Due to the fact that magnesium hydroxide is thermodynamically more stable than magnesium oxide in aqueous environment, the exposed surface is typically composed of magnesium hydroxide [9],[36]. Of these three reactions, only the anodic dissolution and hydration of bulk magnesium are electrochemically-dependent, and both hydration of magnesium and magnesium anions are pH-dependent. Hydration of magnesium oxide is purely a chemical reaction, independent of pH and potential. Thus, due to the fact that the solubility of $Mg(OH)_2$ at room temperature is on the order of a millimolar, the system tends to self-buffer in a pH range of 8.5-10.

$$Mg \rightarrow Mg^{2+} + 2e^{-} \qquad E_0 = -2.37\,V + 0.0295\log[Mg^{2+}] \qquad (3.1)$$

$$Mg + H_2O \rightarrow MgO + 2H^{+} + 2e^{-} \qquad E_0 = -1.86 - 0.059\,pH\,V \qquad (3.2)$$

$$MgO + H_2O \leftrightarrow Mg(OH)_2 \qquad (3.3)$$

$$Mg^{2+} + H_2O \leftrightarrow MgO + 2H^{+} \qquad \log[Mg^{2+}] = 16.95 - 2pH \qquad (3.4)$$

As Mg is anodically dissolved, the following cathodic reaction will proceed at impurity sites, intermetallic particles, or secondary phases more “noble” to pure Mg:

$$2H_2O + 2\,e^{-} \rightarrow H_2 + 2OH^{-} \qquad E_0 = 0.00 - 0.059pH\,V \qquad (3.5)$$

Magnesium is also known for displaying an electrochemical phenomena known as the negative difference effect (NDE), where the cathodic reaction continues to proceed during anodic polarization. For typical metallic polarization behavior, as the potential is increased, the cathodic reaction (e.g. water reduction) rate will slow while the anodic reaction (e.g. metallic dissolution) rate increases. This means the hydrogen evolution rate at the surface at the free corrosion potential is higher than the hydrogen evolution rate at anodic potentials, and the difference between these two values is positive. In the case of magnesium, however, as the potential is increased, the cathodic reaction rate will actually increase as the anodic reaction rate increases. As a result, the difference between the hydrogen evolution rate at the surface at the free corrosion potential and the hydrogen evolution rate at anodic potentials is negative. This phenomena originally led to theories of univalent Mg dissolution, although divalent Mg dissolution is generally agreed upon

within the scientific community [5]. Regardless, the NDE is still not well understood and continues to serve as a topical issue of interest.

3.2.3. Oxide Film Formation

Characterization of quasi-passive film formation on magnesium has been performed using scanning electron microscopy (SEM), X-ray diffraction, and electron diffraction, where it has been found that the initial air-formed magnesium oxide layer is quickly replaced by epitaxial growth of crystalline magnesium hydroxide [37]–[39]. Several studies have shown the thickness and composition of the quasi-passive film to be influenced by alloy composition, as decreasing film thickness and presence of Al has been found as a function of increasing Al concentration in Al-containing alloys [27],[40]. The film structure may also be sensitive to processing methods, as some studies have reported morphology and corrosion rate changes following rapid solidification processing [36],[41]. These kinds of effects may be more closely related to size and spacing of secondary phases and intermetallic particles, however. Reports by Unocic have also found the presence of $MgCO_3$ in addition to the commonly noted components of $Mg(OH)_2$ and MgO when using transmission electron microscopy (TEM), X-ray photoelectron spectroscopy (XPS), and secondary ion mas spectroscopy (SIMS) to examine the surface of ultrahigh purity Mg films formed in room temperature water [42]. Additionally, impurity metal precipitates were found within the film for Mg-alloys. Thus, while the exact mechanism behind the formation of the quasi-passive film is not well-

understood, it is generally accepted that a layered combination of $MgO/Mg(OH)_2$ will form on the surface of Mg and Mg-alloys in aqueous solutions, with the presence of "noble" metal precipitates when impurities are present.

3.2.4. Rotating Disk Electrode

While countless aqueous free corrosion tests have been performed on Mg and Mg-containing alloys, very little work has been done using rotating disk electrode (RDE) systems. Rotating electrodes improve mass transport while reducing concentration polarization through mixing in the form of steady laminar flow over the sample surface [14]. At low rotations speeds, laminar flow is maintained throughout the entire region of flow. At sufficiently high rotations speeds, however, the region of laminar flow becomes limited to the boundary layer adjacent to the sample surface, producing turbulent flow conditions that can be used to simulate erosion corrosion [14],[43],[44]. Figure 3.3. shows a typical RDE setup, where laminar flow across the sample surface is induced by rotating the sample, working to minimize the diffusion boundary layer at the sample surface. While Bender [45] and Marco [46] have used RDE setups to perform polarization experiments on Mg and Mg-containing alloys, no morphology studies or accelerated corrosion testing has been performed using RDE. As an accepted means of performing "accelerated" long-term free corrosion studies, RDE experiments would provide a valuable means of observing the long-term corrosion behavior of Mg and Mg-containing alloys in aqueous environments.

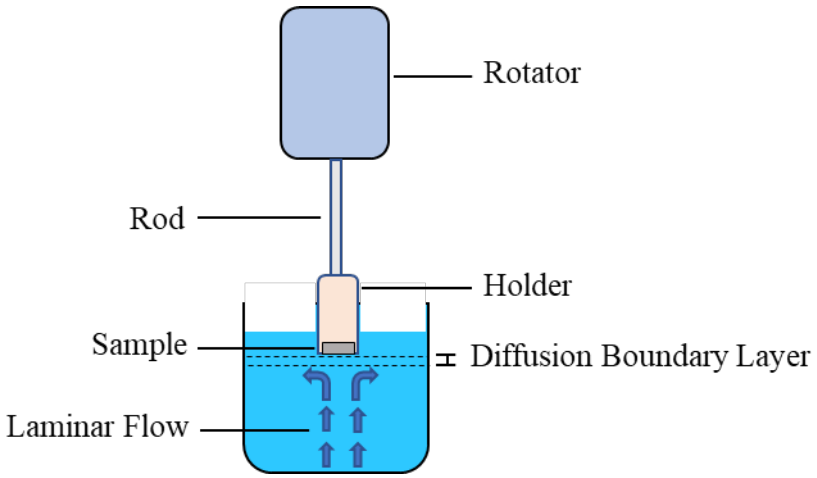

Figure 3.3. Diagram of RDE system.

3.2.5. Ionic Liquid Dissolution

For the purpose of studying a simpler Mg dissolution mechanism in absence of significant surface cathodic activity, the dry conditions produced in ionic liquid (iL) in argon atmosphere provides the ideal environment. Ionic liquids are composed of organic salts, making them aqueous-free solutions comprised entirely of ions. One of these ions will be characterized by a bulky, asymmetric structure, preventing strong ionic interaction between the electrolyte constituents [1]. This prevents the formation of the normally densely packed crystal lattice characteristics of salts (i.e. NaCl), resulting in the low melting temperatures (below 100°C) characteristic of ionic liquids [1]. These low melting points, in addition to their high ion conductivity, low volatility, and good thermal stability, make iLs suitable for a variety of electrochemical applications [1]. Primarily, research performed using Mg in ionic liquid is focused on energy [47],[48] and coating

applications [18],[49]–[57], although work performed by Qing Chen and Sieradzki [58] reports the use of a choline-chloride and urea (ChCl-Urea) eutectic mixture for magnesium dissolution from Mg-Cd alloys to form bi-continuous Cd structures. Results from this work show ChCl-Urea iL to aggressively attack the MgO surface film, allowing for dissolution of Mg from Mg-rich Mg-Cd alloys and successful production of uniform bi-continuous porous morphology. Chen et. al. also reports 1-Butyl-3-MethylImidazoliumm bis-Trifluoromethylsulfonat (BMImTfSI) as an unsuitable iL for dissolution of Mg owing to the inert nature of MgO in this electrolyte. From this, it is expected that a ChCl-Urea eutectic mixture would make a suitable electrolyte for Mg dissolution studies, the structure of which is shown in Figure 3.4.

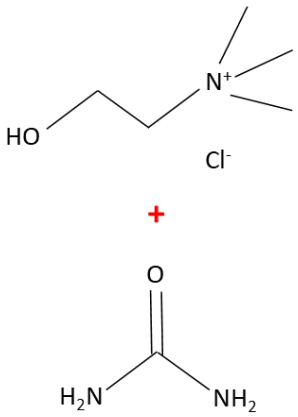

Figure 3.4. Molecular structure of choline chloride (top) – urea (bottom).

3.3. Methods

3.3.1. Alloy Characterization and Fabrication

Component phases.—99.95% commercially pure (CP) magnesium (Alfa Aesar) and 99.9999% pure Al sheet (Alfa Aesar) were used in elemental metal studies. $Mg_{17}Al_{12}$ β-phase was supplied by Stéphane Mathieu (Université de Lorraine, Nancy France).

Binary Phase alloys.—Mg-Al alloys of variable Al concentration (2, 5, and 8 at% Al) were synthesized by the Ames Lab. To ensure solid solution and elimination of β-phase precipitates, samples were annealed in He/Ar at 425°C for 6 days, followed by room temperature water quench. This procedure was successful in Mg-2%Al and Mg-5%Al, referred to herein as αMg-2%Al and αMg-5%Al, respectively. Owing to the slow cooling rate of the water quench, the procedure failed to eliminate all β-phase precipitates in the case of Mg-8%Al, which contains Al concentration much closer to the solubility limit (~11.5 at.% Al). As such, experiments conducted on Mg-8%Al were performed with the understanding that some β-phase precipitates are present on the sample surface.

Synthetic alloys.— "Synthetic" alloys were produced using photolithography techniques. The photolithographic mask pattern (Chrome/Quartz, Photo Sciences) was designed to produce 5% areal coverage of Al. The mask was used during photoresist development to

reveal 7.3 μm diameter holes of exposed substrate located on the corners and edges of a 50 μm square lattice. The newly exposed areas were sputtered for 1 minute under vacuum using an ultra-high purity Ar plasma to remove any residue and oxide followed by 100 nm Al layer deposition using Mg (99.95%, Alfa Aesar) and α-Mg-5%Al substrates. Unlike other tested samples, no additional sample preparation was performed on synthetic alloys in order to preserve the surface patterning.

Characterization.—Surface morphologies were characterized using X-ray diffraction spectroscopy (XRD), scanning electron microscopy (SEM), and energy dispersive X-ray spectroscopy (EDS) on an etched mirror surface finish. Following completion of the standard sample preparation procedure outlined in the subsequent section, a mirror finish was obtained by continued polishing using a series of oil-based diamond slurries down to 0.5 μm particle size, followed by ethanol rinse. To accentuate the surface morphology, an acetic picral etchant was used to selectively attack grain boundaries and secondary phases on the surface [59]. Compositions of all alloys and component phases were confirmed using X-ray diffraction spectroscopy (XRD), shown in Figure 3.7. Phases were identified using scanning electron microscopy (SEM), and secondary confirmation of surface compositions was performed using energy dispersive X-ray spectroscopy (EDS).

3.3.2. Sample Preparation

Samples were prepared by sanding the surface to 1200 grit using carbide paper and ethanol lubricant, followed by ethanol rinse and drying under nitrogen gas flow.

3.3.3. Aqueous Free Corrosion

Corrosion potential monitoring.—Kapton tape was used to encase samples with copper tape backing, providing an extended electrical connection while maintaining an exposed surface area of 0.124 cm^2. Samples were immersed in 30 mL 3.5% w/v NaCl. The corrosion potential monitoring experiment for each sample was comprised of four components. To begin, corrosion potential monitoring was performed for 1 minute, immediately followed by linear sweep voltammetry (LSV) from lower limit –0.1 V (vs. initial corrosion potential) to upper limit 1.0 V (vs. initial corrosion potential) at 10mV/s using Ag^+/AgCl reference and Pt disk counter electrode. Corrosion potential monitoring was then performed for 20 hours, followed by an additional LSV using the same settings.

Rotating disk electrode (RDE) free corrosion.—Cylindrical samples of 5 mm diameter were individually prepared by free immersion in 30 mL of 3.5% NaCl for variable duration at 1600 rpm with 0.196 cm^2 exposed surface area using a Pine RDE710 Rotator. Samples were then soaked in ultra pure (UP) water for 20 minutes to reduce corrosion product and left to air dry in a desiccator overnight.

3.3.4. Atmospheric Corrosion

Contact angle evolution.—Prepared samples were freely corroded for variable duration, rinsed in UP water, and left in a desiccator overnight to dry. A pipette was then used to place a 5 µL drop of UP water on the surface and imaged using a Nikon D3200 camera with lens extension tube set. The contact angle between the droplet and sample surface was measured using ImageJ software.

20 hour pH monitoring.—Prepared samples were encased in Kapton tape with exposed surface area of 0.124 cm^2. Samples were then immersed in 30 mL 3.5 w/v% NaCl for 20 hours while the pH was monitored by standard glass electrode positioned near the corroding surface.

Surface pH monitoring.—The surface pH within a droplet of UP water on sample surfaces was observed using a universal dye-indicator in ultrapure water suspension. The dye-indicator solution was synthesized via dye extraction from universal pH strips (Advantec) [15]. A drop of universal dye-indicator solution was then placed on a prepared sample surface, and images were taken using a Nikon D3200 camera with lens extension tube set approximately every four seconds until pH stabilization was observed.

3.3.5. Rate Kinetics

Prepared samples were encased in Kapton tape and parafilm to maintain 0.124 cm^2 exposed surface area. Samples were then freely corroded in 2 mL of 3.5% NaCl for 20 min, 80 min, 180 min, 240 min, 4 hr, and 20 hr durations in 15 mL trace metal-free tubes (VWR). This procedure was repeated in an additional solution of 2 mL 3.5% NaCl + pH 9 buffer solution in the case of Al. Inductively coupled plasma mass spectroscopy (ICP-MS) was used to record Mg and Al concentrations in the electrolyte following free corrosion.

3.3.6. Ionic liquid dissolution

Corrosion potential of synthetic alloys and component phases in ionic liquid. —Prepared samples were encased in Kapton tape with copper tape backing, providing an extended electrical connection while ensuring an exposed surface area of 0.124 cm^2. Owing to previous results by Qing Chen et. al. reporting successful targeted dissolution of Mg in 1:2 molar ratio choline-chloride:urea (CC-urea) at 150°C in inert argon environment [60], all ionic liquid dissolution was performed using 1:2 molar ratio CC-urea. Samples were immersed in 15 mL CC-urea at 150°C in inert argon environment. Polarization behavior was observed by performing LSV from lower potential limit -600 mV to upper potential limit 600 mV (vs. Al^{3+}/Al) at 10 mV/s using Al wire quasi-reference and Pt mesh counter electrode.

Potentiostatic anodic dissolution. —Prepared samples were encased in Kapton tape with copper tape backing, providing an exposed surface area of 0.124 cm^2, followed by immersion in 15mL CC-urea at 150°C in argon. Anodic dissolution was then driven by potentiostatic hold at -100 mV (vs. Al^{3+}/Al) for variable duration using Al quasi-reference and Pt mesh counter electrode. Following dissolution, CC-urea was rinsed from the surface using 1.0 M propylene carbonate heated to 150°C, followed by acetonitrile.

3.4. Results and Discussion

3.4.1 Characterization

Following the acquisition of AZ31B, AM60 and AZ91D commercial alloys, their microstructure and composition were characterized using SEM, EDS and X-ray diffraction (XRD), the results of which are reported in Figures 3.5, 3.6. and 3.7., respectively. The XRD results in Figure 3.7.a as well as EDS were used to identify the bright contrast secondary phases present in the commercial alloys such as the β $Mg_{17}Al_{12}$ phase in AM60 and AZ91D as well as $MnAl_3$ particulates in AZ31B. They were also used to verify the Al concentration in the solid-solution α-phase.

Type	Alloy	Composition (at.%)							
		Mg	Al	Cu	Fe	Ni	Zn	Mn	Si
Commercial	AZ31B	96.73	2.70	0.019	0.002	0.002	0.373	0.088	0.087
	AM60	94.25	5.39	0.004	0.002	0.001	0.082	0.185	0.087
	AZ91D	90.72	8.77	0.011	0.002	0.001	0.255	0.147	0.087
Binary Phase	α-Mg 2 at.% Al	98	2	0	0	0	0	0	0
	α-Mg 5 at.% Al	95	5	0	0	0	0	0	0
	Mg 8 at.% Al	92	8	0	0	0	0	0	0

Table 3.2. Compositions of studied commercial and binary phase alloys, along with component phases.

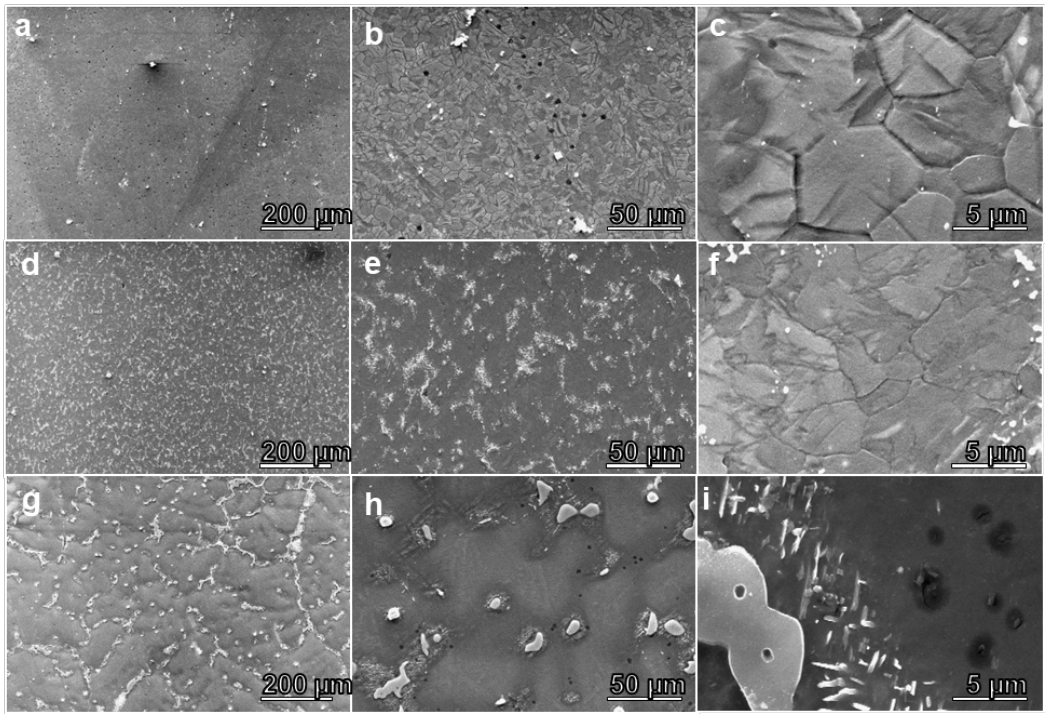

Figure 3.5. Microstructural characterization of untreated commercial alloys at various magnifications using SEM for a, b, c) AZ31B, d, e, f) AM60 and g, h, i) AZ91D.

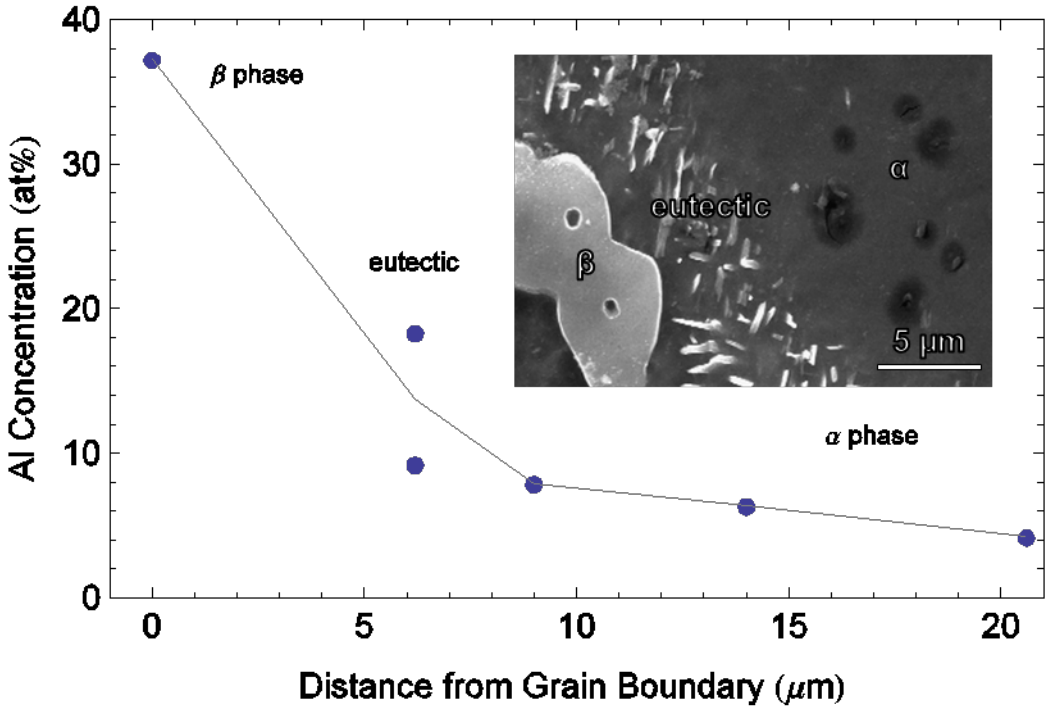

Figure 3.6. Distribution of Al concentration in a balance of Mg within a representative AZ91D grain. The $Mg_{17}Al_{12}$ β phase is proximal to the grain boundary, a solid solution α phase 4-8 at.% Al is located inside the grain, and between the two phases exists a eutectic region consisting of both α and β phase. The lowest Al concentration is found at the center of the grain, and it gradually increases outward toward the grain boundaries.

In Figure 3.7.a, reference patterns for Mg, α-Mg-10% Al, β $Mg_{17}Al_{12}$ and $MnAl_3$ phases were superimposed over the data and shown in the insets plotted in the two regions most prominent for the listed phases. AZ31B exhibited a peak between Mg and α-Mg-10% Al, which is in good agreement with the 2.7 – 3.2 at.% Al probed by EDS. Also, as shown in the second inset graph, a small peak is exhibited associated with $MnAl_3$, as displayed by the bright particulates in Figure 3.5.b located near the boundaries of 5-10 μm size grains (see Figure 3.5.c). For AM60, a peak was observed between Mg and α-Mg- 10% Al, supporting the ~ 4.0 at.% Al measured by EDS. A small peak is exhibited associated with the β-phase, as displayed by the bright particulates in Figure 3.5.f located near the

boundaries of 2-5 μm size grains. AZ91D exhibited a high intensity peak associated with the β-phase as well as a small peak between Mg and α-Mg- 10% Al consistent with the 4.2-7.9 at.% Al measured by EDS across grain sizes ranging from 50-100 μm. This relatively large distribution of Al within the AZ91D grains is plotted in Figure 3.6. as measured by EDS. The lowest Al concentration is found at the center of the grain, approximately 4.2 at.% Al, and it gradually increases radially outward toward the grain boundaries to a maximum of approximately 7.9 at.% Al. This is consistent with results obtained by Ambat et. al [61]. Large secondary β phases reside at the grain boundary, and between the α and β phases, a eutectic region exists containing both phases.

XRD was also used to verify composition of solid solution solid solution α phase containing approximately 2, 5 and 8 at.% Al (Figure 3.7.b), β phase with and without 1.0 at.% Zn (Figure 3.7.c) as well as $MnAl_3$ (Figure 3.7.d). The peaks exhibited in the XRD spectra agree with the desired phases. Furthermore, the peak shift between reference patterns for Mg and α Mg- 10% Al are in good agreement with the desired range of Al composition for the solid solution α Mg-Al alloys.

Synthetic alloy morphology and composition was characterized using SEM and EDS elemental mapping. Figure 3.8.b confirms successful patterning of islands using photolithography. Higher magnification also reveals even deposition of Al with ~150 nm grain size (Figure. 3.8.a). EDS elemental mapping confirms Mg substrate and Al island

composition. Presence of a carbon ring surrounding the Al island edges is likely residual photoresist.

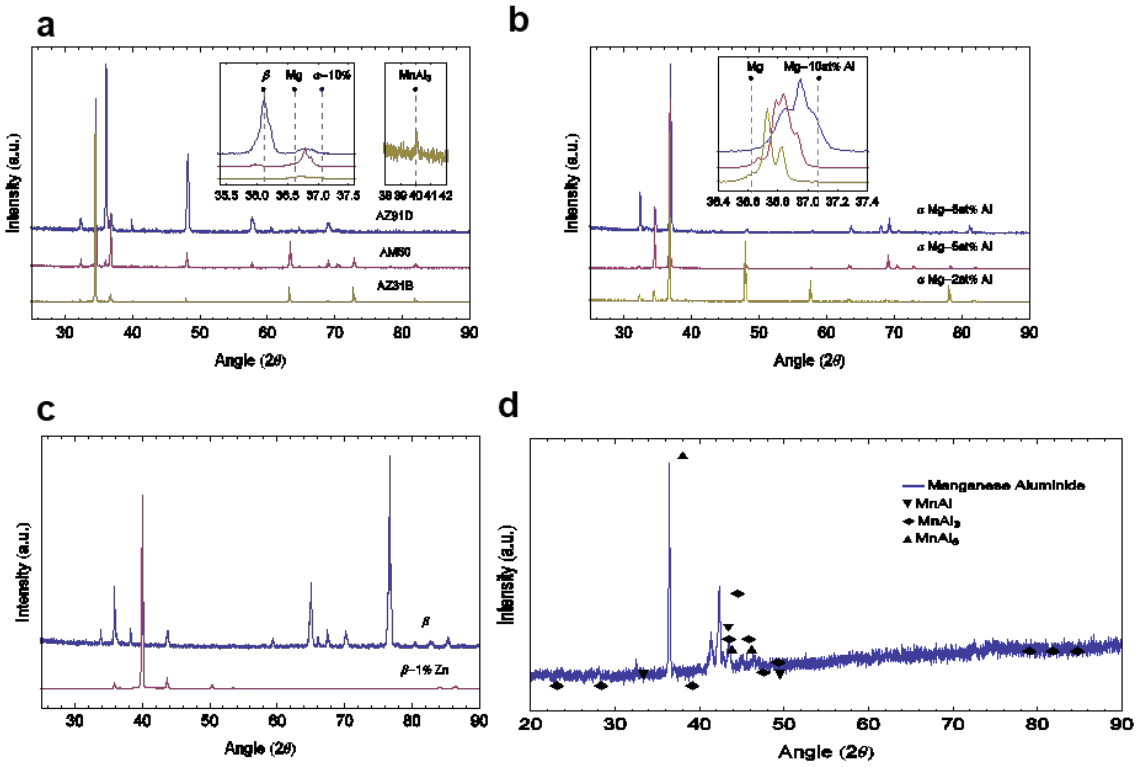

Figure 3.7. XRD patterns for a) commercial alloys AZ91D, AM60 and AZ31B, b) solid-solution α phase samples containing approximately 2-8 at.% Al, c) $Mg_{17}Al_{12}$ β phase with and without 1% Zn and d) manganese aluminide.

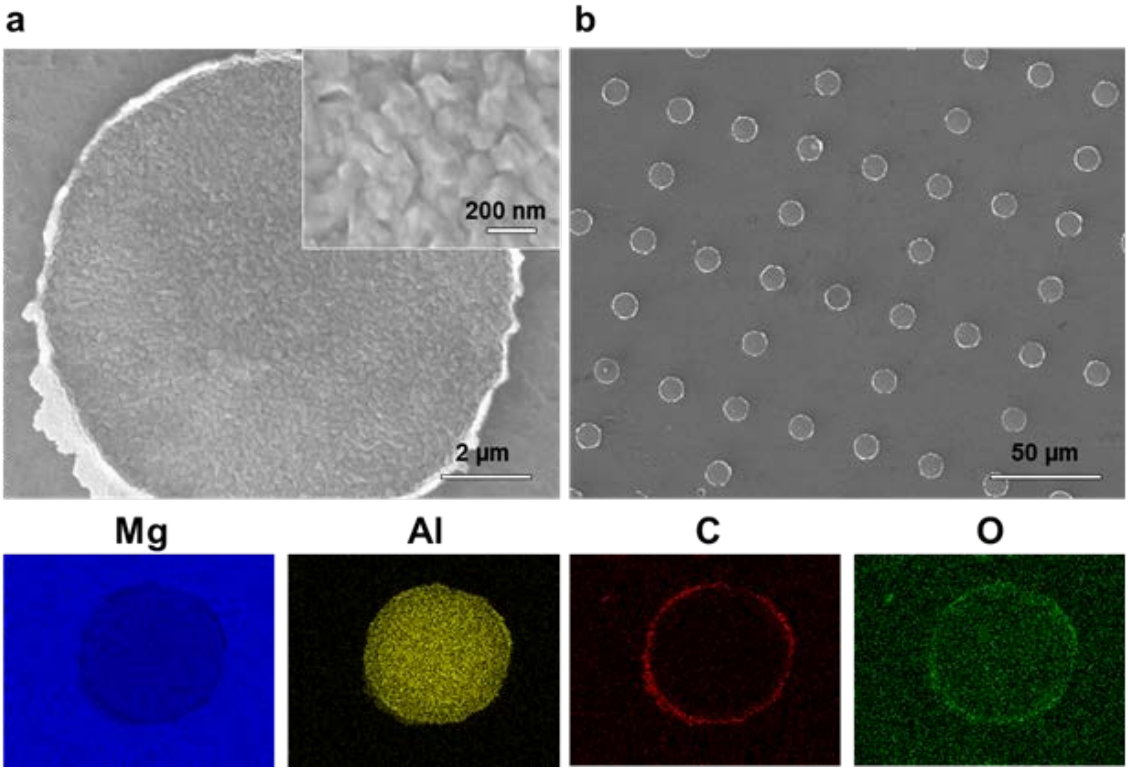

Figure 3.8. SEM surface morphology of 5%, 100 nm Al coverage on pure Mg substrates that underwent 1 min sputtering during photolithography at a) higher magnification showing the Al island including the deposit texture (inset) and b) lower magnification showing the overall pattern. EDS areal mapping was performed on the aluminum island in a) to show the elemental mapping of Mg, Al, C and O.

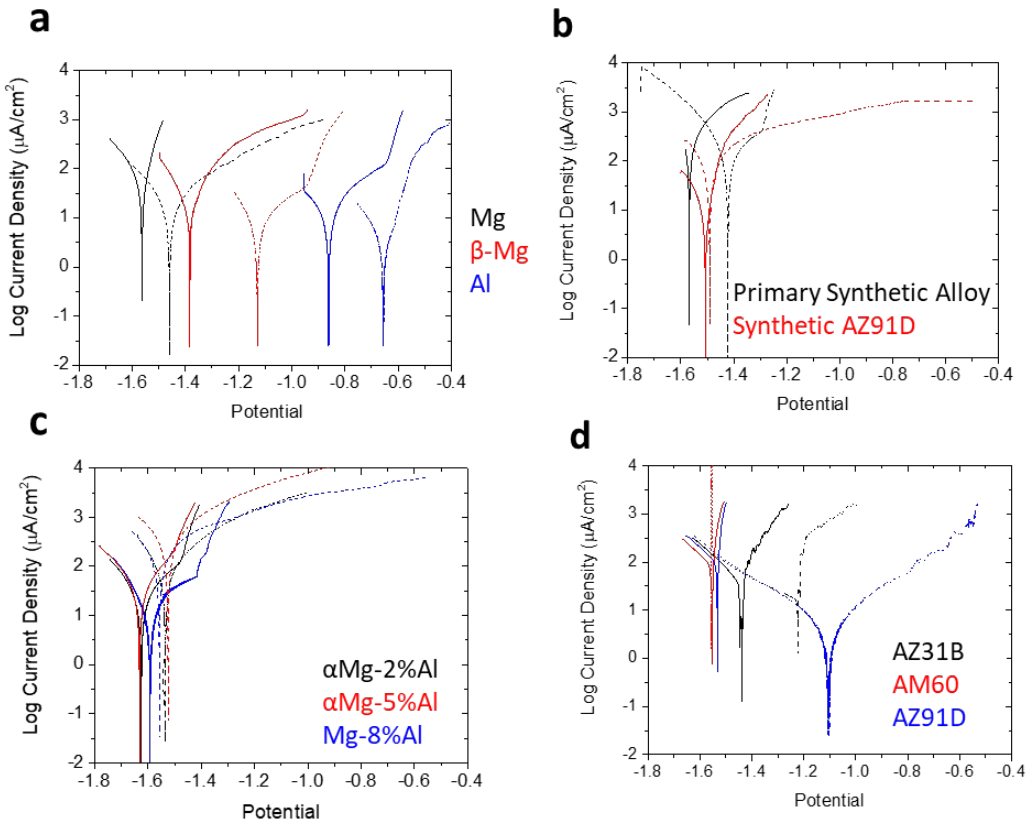

Figure 3.9. Shift in corrosion potential (vs. Ag^+/AgCl) for (a) component phases, (b) synthetic alloys, (c) binary-phase alloys, and (d) commercial alloys during 20 hour free immersion in 3.5% NaCl. Solid lines indicate polarization results after 1 min immersion while dotted lines indicate polarization results after 20 h immersion. LSV was performed from lower limit -0.1 V (vs. initial corrosion potential) to upper limit 1V (vs. initial corrosion potential) at 10 mV/s using Ag^+/AgCl reference electrode and Pt mesh counter electrode.

CORROSION POTENTIAL V.vs Ag^+/AgCl; 3.5% NaCl			
SAMPLE	1 minute	20 hours	Δ CP
Primary Synthetic	-1.60	-1.35	0.25
Synthetic AZ91D	-1.51	-1.49	0.02
αMg-2At%Al	-1.62	-1.53	0.09
αMg-5At%Al	-1.63	-1.52	0.11
Mg-8At%Al	-1.59	-1.56	0.03
AZ31B	-1.44	-1.22	0.22
AM60	-1.55	-1.56	-0.01
AZ91D	-1.53	-1.11	0.42
Al	-0.86	-0.66	0.20
β-Mg	-1.38	-1.13	0.25
Mg	-1.56	-1.46	0.10

Table 3.3. Summary of corrosion potential shifts (vs. Ag^+/AgCl) for component phases and binary-phase alloys during 20 hour free immersion in 3.5% NaCl**.**

Anodic Branch Slope Change mV.vs CP; 3.5% NaCl		
SAMPLE	1 minute	20 hours
αMg-2at%Al	150	-
αMg-5at%Al	130	-
Mg-8at%Al	170	-
Al	210	-
β-Mg	-	190

Table 3.4. Summary of pitting potentials for component phases and binary-phase alloys during 20 hour free immersion in 3.5% NaCl. CP Mg and commercial phases have not been included, as they do not display pitting behavior.

3.4.2. Aqueous Free Corrosion

Polarization behavior of binary-phase alloys and component phases.— Corrosion behavior of binary and commercial alloys during 20 hour free immersion in 3.5% NaCl was characterized using polarization testing (Figure. 3.9.b-c). To establish an expected

behavior regime, polarization testing was also performed on component phases: CP Mg, β-phase Mg, and 99.999% pure Al (Figure. 3.9.a). A complete summary of observed corrosion potentials is provided in Table 3.3.

Corrosion potentials ranged from -1.56 V vs. Ag^+/AgCl (initial immersion of CP Mg) to -0.66 V vs. Ag^+/AgCl (20 hour immersion of Al) for component phases, all of which displayed positive potential shift and decreasing corrosion kinetics during 20 hour free immersion. Binary alloys displayed corrosion potentials characteristic of CP Mg, along with small positive potential shifts during free immersion. Contrary to component phases behavior, binary alloys exhibited increasing corrosion kinetics. Commercial alloys generally maintained similar corrosion kinetics throughout 20 hour immersion with a noble corrosion potential shift. Exceptions include AM60, which maintained similar corrosion potential throughout immersion time, and AZ91D, which displays decreased corrosion kinetics after 20 hr free immersion.

The primary synthetic alloy corrosion potential shifts +250mV during 20 hour immersion. Interestingly, in comparing the behavior of the synthetic alloy containing 5 % area fraction of Al with the α-phase 5 % Al alloy, the initial corrosion potentials are similar, but after 20 hours there is a significantly larger increase in the corrosion potential of the synthetic alloy (0.25 V vs. 0.11 V). The initially measured corrosion potentials of synthetic and commercial AZ91D are nearly identical. Unlike commercial AZ91D,

however, synthetic AZ91D experiences very little positive shift in the corrosion potential (30 mV) after 20 hour free immersion.

In the case of Al and binary phase alloys, the one-minute anodic branch exhibits an increase in slope within a few hundred millivolts of the corrosion potential, as characteristic of pitting in Al (Table 3.4) [62],[63]. This feature is not present in the anodic branch of Al or binary phase alloys following long term immersion. In the case of the Al-containing β-phase Mg, however, the sharp slope increase occurs only after 20 hour immersion, possible suggesting Al surface enrichment and subsequent pitting. These pitting potentials have been summarized in Table 3.4. Although exact pitting potentials of Mg and Mg-Al alloys have proven difficult to characterize in aqueous chloride [64]–[66], values obtained for Al are consistent with those reported in the literature [62],[67],[68].

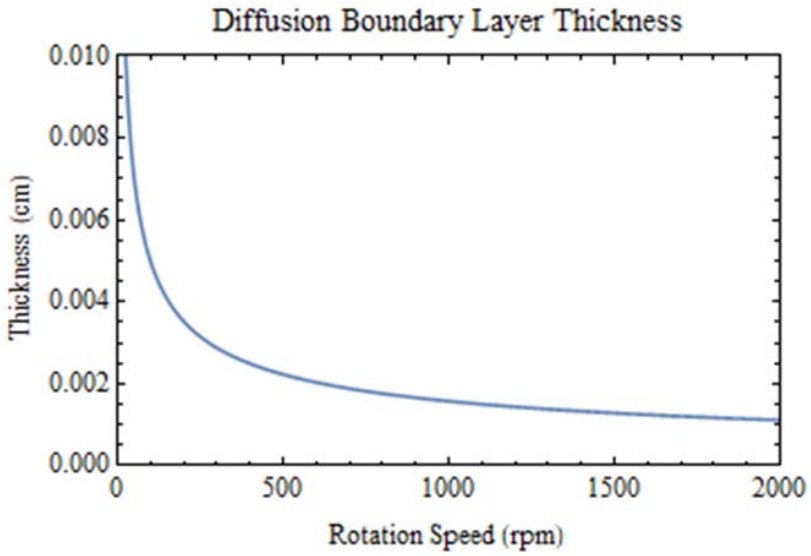

Figure 3.10. Diffusion boundary layer thickness as a function of rotation rate evaluated from $\delta = 11.1(\frac{\nu}{RPM})^{0.5}$.

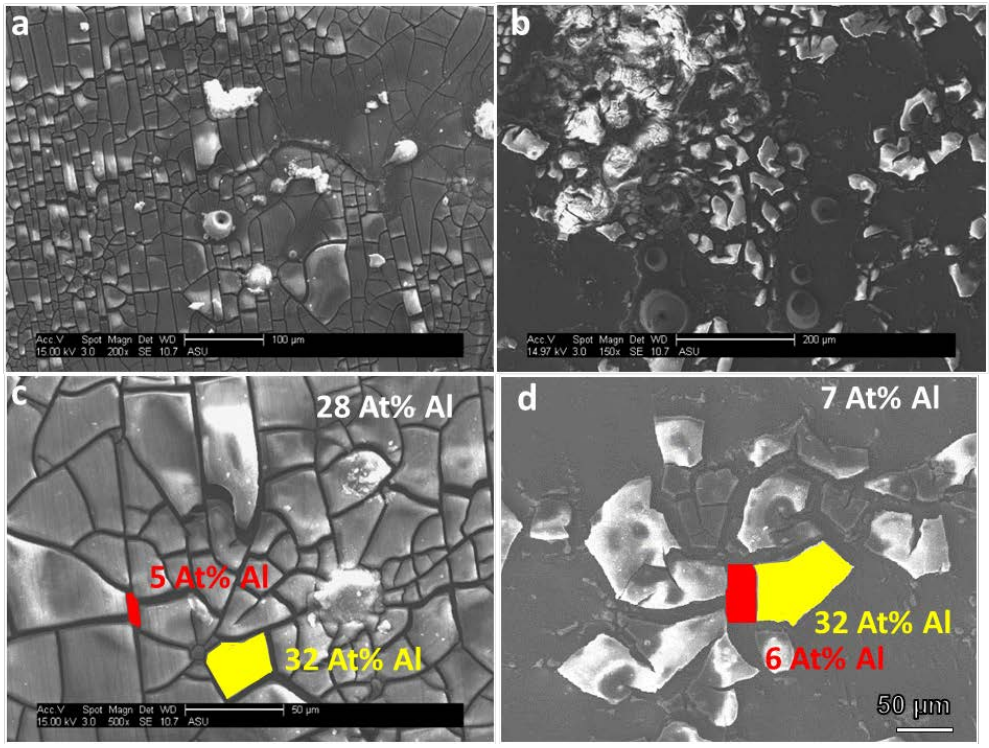

Figure 3.11. SEM imaging of Mg-2%Al (left panel) and Mg-5%Al (right panel) following a 20h immersion in 3.5% NaCl at 1600 rpm at increasing magnification. Higher magnification image (bottom panel) includes EDS data of Al normalized to Mg for the exposed substrate area between platelets (red), platelet surface (yellow), and overall composition (white).

Rotating disk electrode effect on aqueous corrosion.—A rotating disk electrode (RDE) cell was used to simulate long-term corrosion behavior in binary-phase alloys. The use of the RDE experimental design provides continuous laminar flow along the electrode surface, simultaneously minimizing the diffusion boundary layer and increasing the concentration gradient. The diffusion boundary layer thickness can be calculated using Equation 3.6 [69]:

$$\delta(\omega) = 1.61 D_0^{\frac{1}{3}} \omega^{-\frac{1}{2}} \nu^{\frac{1}{6}} \tag{3.6}$$

where δ is the boundary layer thickness (cm), D_0 is the diffusion constant $\left(\frac{cm^2}{s}\right)$, $\omega = \frac{\pi f}{30}$ is the angular frequency ($rotation/min$), and v is the kinematic viscosity of the solution $\left(\frac{cm^2}{s}\right)$. As seen in Figure 3.10., at 1600 rpm the diffusion boundary layer thickness is approximately 12μm. Knowing α-Mg-5%Al contains approximately 500μm grain size, an order of magnitude greater than the calculated diffusion boundary layer thickness, we consider the diffusion boundary layer negligible at this rotation frequency.

For 20 hour free immersion in aqueous chloride at 1600 rpm, platelet formation occurs on the surface of both solid solution binary alloys (Figure 3.11). The most noticeable difference between the two compositions using SEM imaging lies in the surface coverage—α-Mg-2%Al displays nearly full platelet surface coverage whereas substrate exposure is more readily apparent in α-Mg-5%Al. Compositional analysis performed using EDS revealed the platelet concentration of both alloys to be approximately 32 at% Al normalized to Mg. As such, the differences in overall surface composition are significant, with overall Al concentration increasing to 28 at% Al and 7at% Al in α-Mg-2%Al and α-Mg-5%Al, respectively.

3.4.3. Atmospheric corrosion

Contact angle evolution.—As a component of atmospheric corrosion studies, the wetting angle of Mg-Al alloys (Mg-5%Al, AZ91D, AM60, and AZ31B) and component phases (Al and Mg) were measured as a function of free corrosion duration. Figure 3.12. shows

representative images for wetting of AZ91D un-corroded and 20 hr corroded sample. One can qualitatively observe the decrease in contact angle. Figure 3.13. shows the exponential decrease in wetting angle with increasing corrosion time for all samples. This is likely due to increased surface roughness with longer corrosion durations. Magnesium surfaces undergo rapid dissolution when exposed to aqueous chloride due to its high susceptibility to corrosion. Magnesium is preferentially dissolved from the surface while more "noble" components, including Al and impurity metals (i.e. Fe, Zn), will remain on the surface until they are undercut. Areas of lower surface energy, such as step and kink sites with fewer nearest neighbors, are preferentially attacked. This combination leads to rapid surface roughening and increased wetting. The effects of surface roughness on the contact angle have been well documented by Wenzel where surface roughness is connected with Young's equation by:

$$cos\theta_W = r\frac{(\gamma_{SV}-\gamma_{SL})}{\gamma_{LV}} = rcos\theta_\gamma \tag{3.7}$$

where θ_W is the contact angle of the roughened surface, r is the roughness ratio factor, γ_{SV} is the interfacial energy of the solid-vapor interface, γ_{SL} is the interfacial energy of the solid-liquid interface, γ_{LV} is the interfacial energy of the liquid-vapor interface, and θ is the contact angle of the geometrically flat surface [70]. From Young's equation we know $\gamma_{SL} > \gamma_{SV}$ for $180° > \theta_\gamma > 90°$ and $\gamma_{SL} < \gamma_{SV}$ for $0 < \theta_\gamma < 90°$. Looking at Equation 3.7, we see that for $180° > \theta_\gamma > 90°$ increasing r results in $\theta_\gamma < \theta_W$ and for $0 < \theta_\gamma < 90°$ increasing r results in $\theta_\gamma > \theta_W$. Our results are consistent with this since

all surfaces show an initial tendency towards wetting with contact angles less than 90° and the contact angle continues to decrease with increasing roughness. Al does not display these effects as rapidly as Mg and Mg-containing alloys, likely due to the protection of the passive Al oxide film. This appears to extend to higher Al-content alloys as well since AZ91D shows slower decay compared with other commercial alloys.

20 hour pH monitoring.—A standard glass electrode was used to monitor pH evolution of component phases, binary-phase alloys, and commercial alloys during 20 hour free immersion in aqueous chloride (Fig. 3.14.). All Mg-containing samples display initial rapid increase in pH with eventual stabilization within pH range 8-10. As expected, after a brief initial pH increase, Al stabilized at approximately pH 6.5 during 20 hour free immersion. Of the binary phase alloys tested, both α-Mg-5%Al and Mg-8%Al display behavior characteristic of CP Mg while α-Mg-2%Al maintains Al-like behavior for the first 10 hours of immersion before stabilizing at pH 9. Commercial alloys also resemble the behavior of CP Mg, with AZ31B displaying slower pH increases.

Surface pH evolution.— Surface pH approximation of binary phase alloys and component phases was performed using universal dye indicator with initial pH 5-6. The color scale for the universal dye indicator is provided in Figure 3.15. Just as in the case of 20 hour pH monitoring, Al remains stable at pH 5-6, and no observable change occurs when a droplet of UP water is applied to the surface (Figure 3.16). CP Mg experiences immediate pH increase as dye indicator is placed on the surface with rapid stabilization at

pH 9 within four seconds (Figure 3.17). As shown in Figures 3.18-22, stabilization within the droplet takes more time in the case of commercial and solid-solution binary alloys. Although stabilization time for solid solution alloys appears independent of concentration, commercial alloys display the opposite trend, with pH stabilization time increasing with increasing Al concentration.

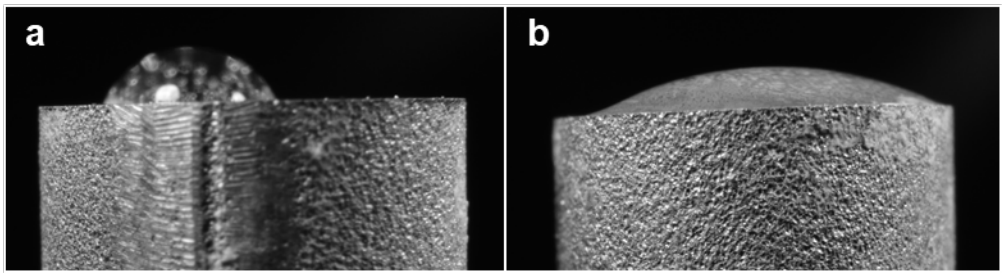

Figure 3.12. Contact angle images of 3.5% NaCl on AZ91D a) un-corroded and b) following 20 hr aqueous corrosion in 3.5% NaCl.

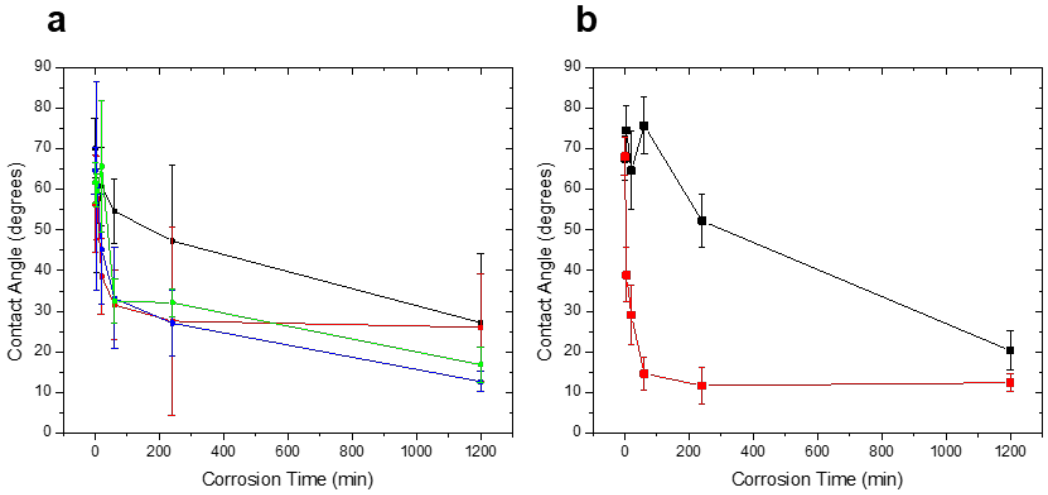

Figure 3.13. Time dependent contact angle of a 5μL of 3.5% NaCl on the indicated sample surfaces (a) Mg-Al alloys: AZ91D (black), AM60 (red), AZ31B (blue), and αMg-5 at.%Al (green) and (b) component phases: Al (black) and Mg (red). Error bars indicate standard deviation of average measurement for 5 samples.

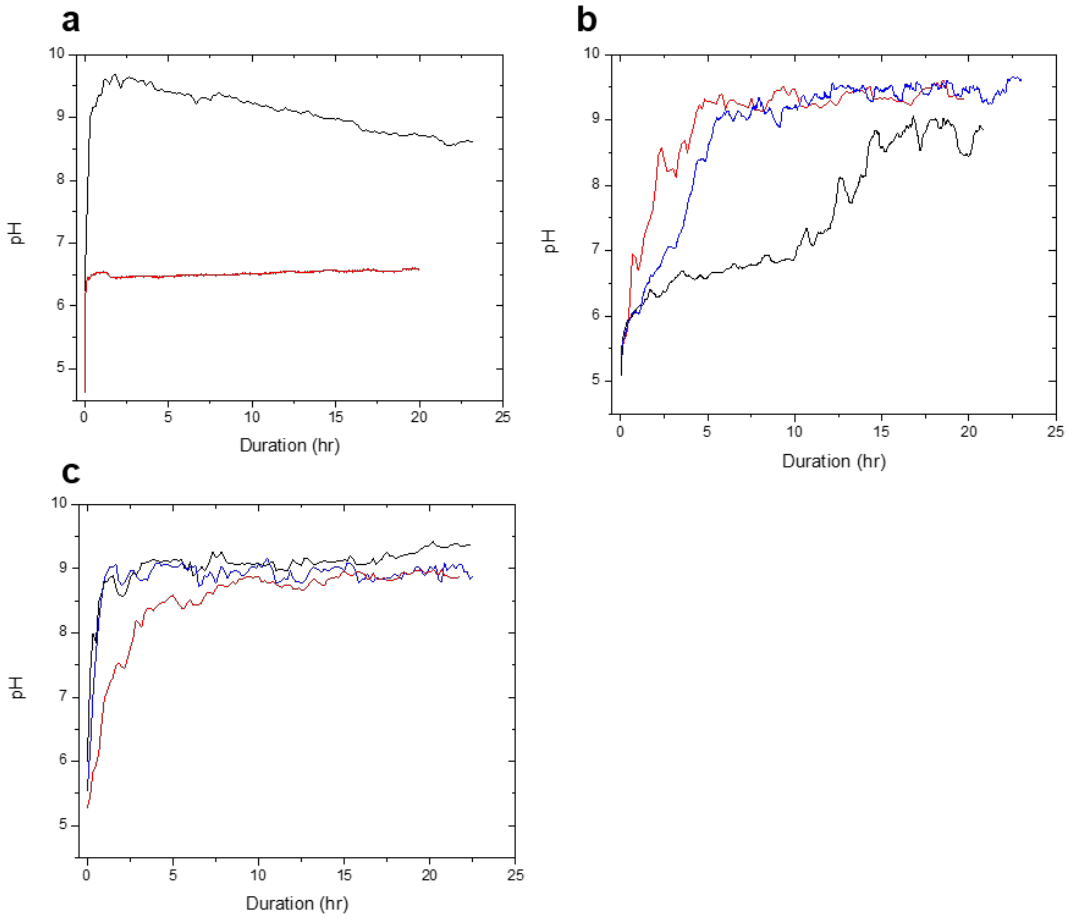

Figure 3.14. Evolution of electrolyte pH under full immersion, free corrosion in 3.5% aqueous NaCl using a standard glass electrode. (a) component phases: Mg (black) and Al (red), (b) binary-phase alloys: α-Mg-2%Al (black), α-Mg-5%Al (red), and α-Mg-8%Al (blue), and (c) commercial alloys: AZ91D (black), AZ31B (red), and AM60 (blue).

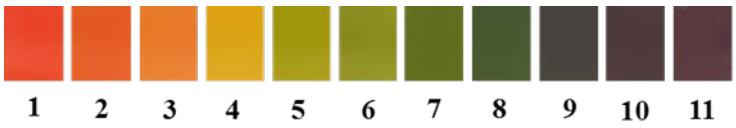

Figure 3.15. Universal dye-indicator color scale (pH 1-11).

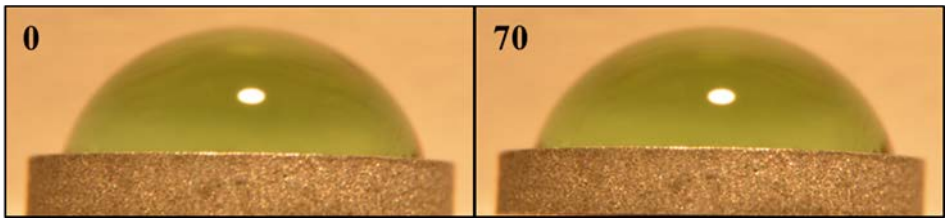

Figure 3.16. Universal dye-indicator in ultrapure water on Al for 70 second free corrosion duration with corrosion time indicated in seconds.

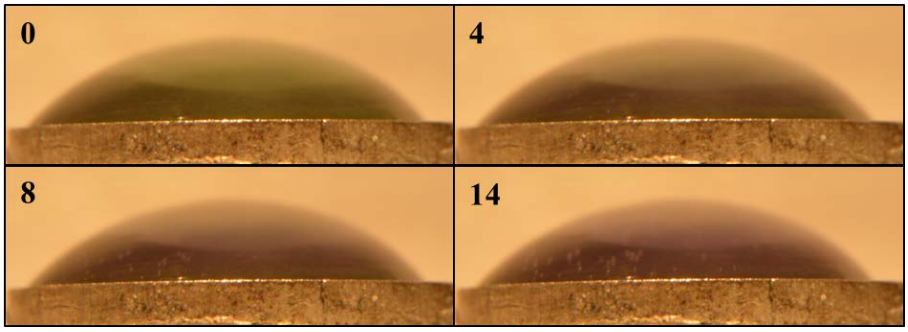

Figure 3.17. Universal dye-indicator in ultrapure water on Mg for 14 second free corrosion duration with corrosion time indicated in seconds.

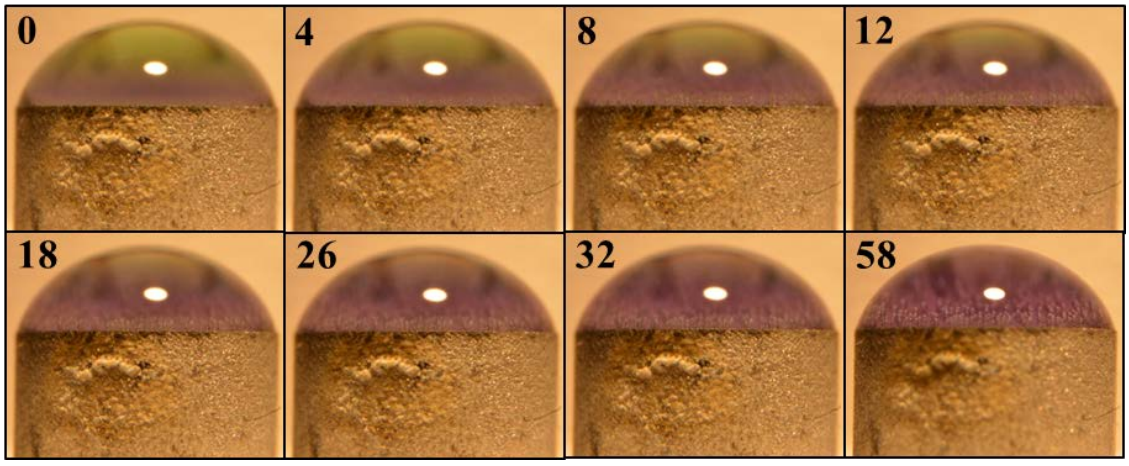

Figure 3.18. Universal dye-indicator in UP water on AM60 for 58 second free corrosion duration. The corrosion time in seconds is indicated in the upper left-hand corner.

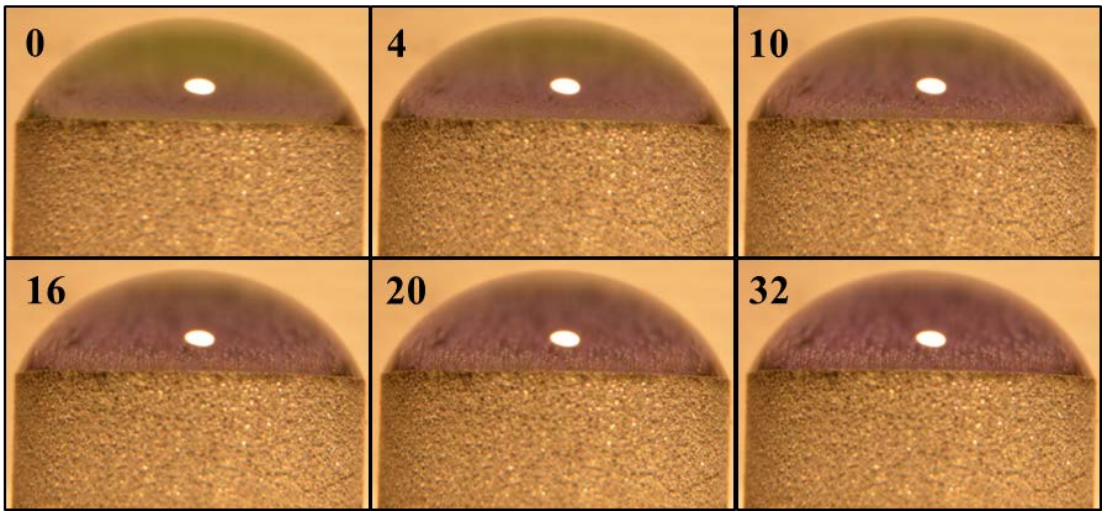

Figure 3.19. Universal dye-indicator in UP water on AZ31B for 32 second free corrosion duration. The corrosion time in seconds is indicated in the upper left-hand corner.

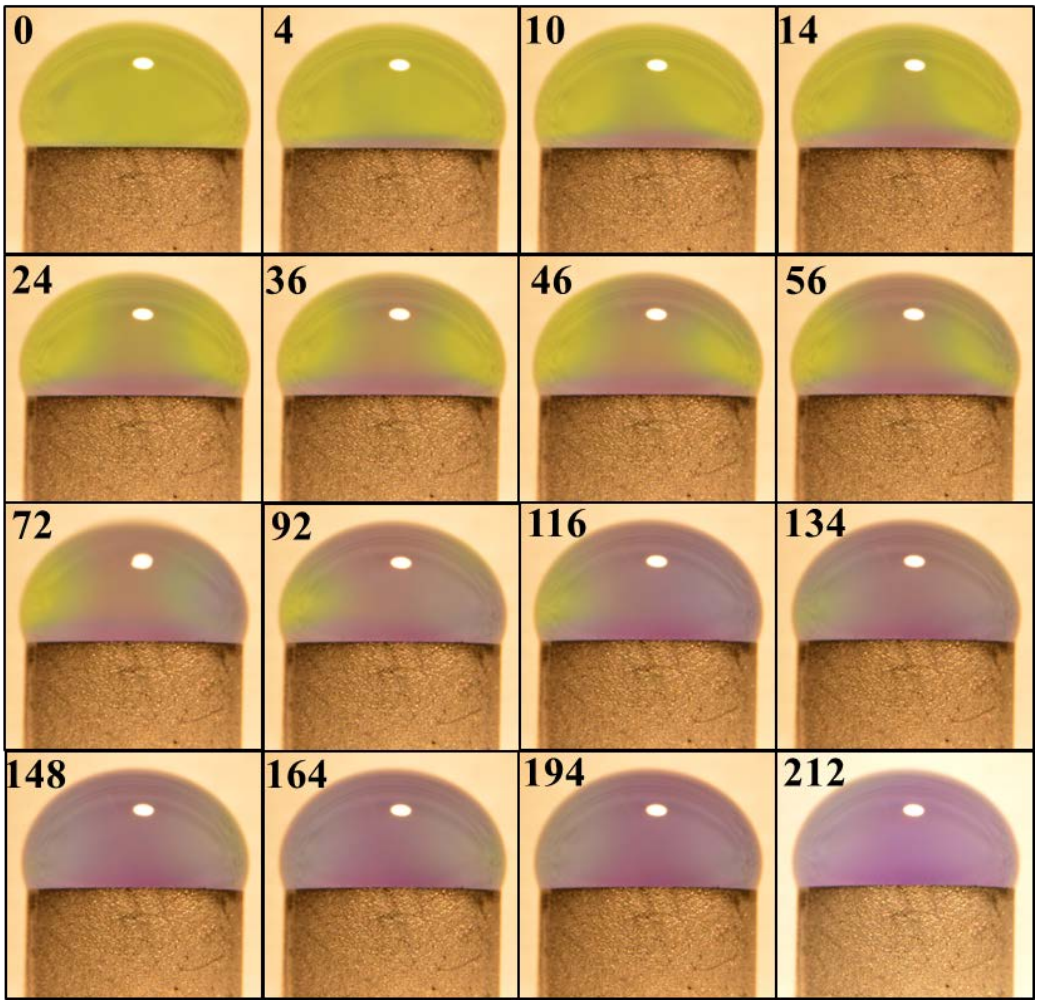

Figure 3.20. Universal dye-indicator in UP water on AZ91D for 212 second free corrosion duration. The corrosion time in seconds is indicated in the upper left-hand corner.

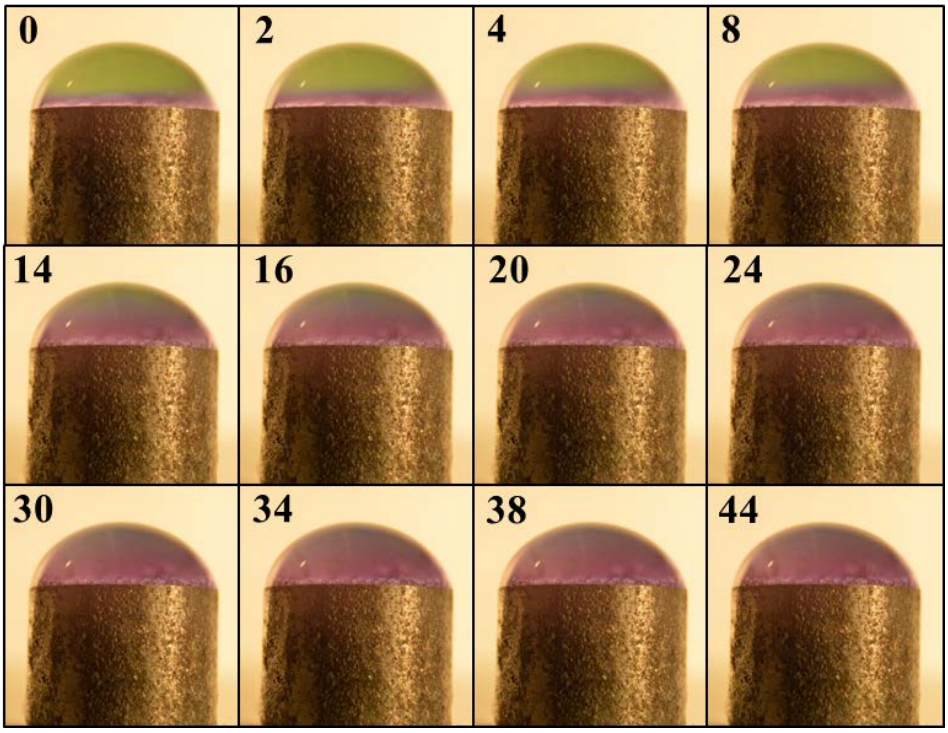

Figure 3.21. Universal dye-indicator in ultrapure water on αMg-2%Al for 60 second free corrosion duration. The corrosion time in seconds is indicated in the upper left-hand corner.

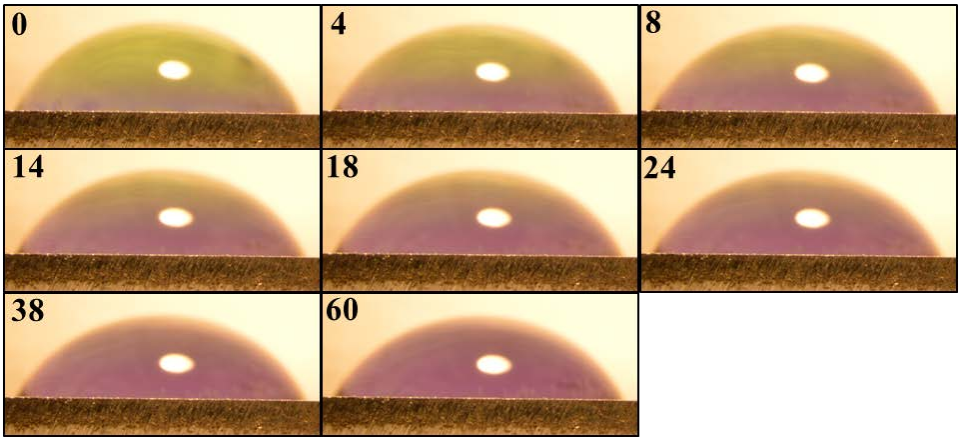

Figure 3.22. Universal dye-indicator in ultrapure water on αMg-5%Al for 60 second free corrosion duration with corrosion time indicated in seconds.

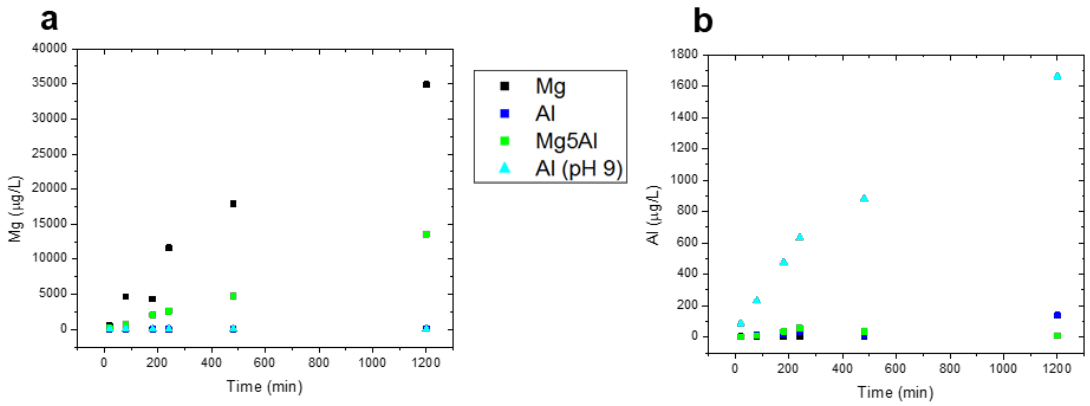

Figure 3.23. ICP-MS determination of chemical dissolution of (a) Mg and (b) Al in 2 mL of 3.5% NaCl over 20 hour immersion in 3.5% NaCl. To determine Al free corrosion rates during localized pH increases, Al dissolution was also performed in 3.5% NaCl + pH 9 buffer.

3.4.4. Rate Kinetics

Oxide dissolution rate kinetics—Expressions for the first-order rate reaction of Mg and Al dissolution were found through experimental observation of the chemical dissolution rates in aqueous chloride using ICP-MS. As reported in Figure 3.23, the Mg and Al dissolution from CP Mg, bulk Al, and α-Mg-5%Al was measured as a function of immersion time in 3.5% NaCl. Al dissolution at elevated pH was also measured to simulate local pH increases that occur during Mg corrosion. When examining the Mg dissolution from CP Mg and Al dissolution from bulk Al, both concentration profiles display a linear trend.

Assuming a first-order rate reaction, the Nernst-Brunner equation can be used to fit the data to a rate kinetics equation:

$$\frac{dC}{dt} = k(C_s - C) \tag{3.8}$$

where k the rate constant (s^{-1}) is equal to $k = \frac{DA}{Vh}$. Here D is the diffusion coefficient ($D \sim 10^{-6}\ cm^2 s^{-1}$), A is the surface area of the dissolving hydroxide ($A = 0.124\ cm^2$), V is the volume of electrolyte ($V = 2\ cm^3$), h is the thickness of the diffusion boundary layer ($h = 0.01\ cm$), C is the concentration, and Mg^{2+} or Al^{3+} in the electrolyte. Using these values, we estimate a rate constant of $k_{Mg} \sim 6 \times 10^{-6}\ s^{-1}$.

In the case of Mg, the saturation concentration is determined by examining the rate-limiting equation for chemical dissolution of Mg:

$$Mg^{2+} + 2OH^- \leftrightarrow Mg(OH)_2 \tag{3.9}$$

Equation 3.9. can be used to obtain the equilibrium constant (K).

$$K = \mathrm{a}_{\mathrm{Mg^{2+}}} a_{OH^-}^2 \tag{3.10}$$

The activity of hydroxide ions (a_{OH^-}), hydrogen ions (a_{H^+}), and magnesium ions ($a_{Mg^{2+}}$) within aqueous chloride are described by the following:

$$a_{OH^-} = \frac{K_w^*}{a_{H^+}} \tag{3.11}$$

$$a_{H^+} = 10^{-pH} \tag{3.12}$$

$$a_{Mg^{2+}} = \gamma_{Mg^{2+}}[Mg^{2+}] \tag{3.13}$$

where K_w^* is the stoichiometric equilibrium constant of seawater ($K_w^* = 6.3 \text{ x } 10^{-14}\ M$ [71]), and $\gamma_{Mg^{2+}}$ is the activity coefficient of magnesium ions (0.255) [72]). The saturation concentration of magnesium ions occurs for the condition $K = K_{sp}$, where $K_{sp} = 1.2 \text{ x } 10^{-11}\ M$ (magnesium hydroxide) [73]. The pH reaches a maximum of approximately 9.3 during magnesium dissolution. Using Equations 3.10-13, we determine the saturated magnesium concentration, $C_{s,Mg} = 2.98\ mM$.

The Al saturation concentration is similarly calculated using the following rate limiting equation for chemical dissolution of Al:

$$Al_2O_3 + H_2O \leftrightarrow 2AlO_2^- + 2H^+ \tag{3.14}$$

Assuming the aluminum oxide is composed of boehmite, the saturation of aluminate ions is described by the following Pourbaix equation [9]:

$$\log[AlO_2^-] = -12.32 + pH \tag{3.15}$$

For pH 9, the saturation aluminum concentration, $C_{s,Al} = 0.4786\ mM$, where $C_{s,Al} = [AlO_2^-]$.

By integrating Equation 3.8, the data can be fit to a first-order rate reaction:

$$\frac{C}{C_s} = 1 - \exp(-kt) \tag{3.16}$$

As shown in Figure 3.24.a, experimentally-derived rate constants were determined for both Mg and Al dissolution from component phases in 3.5% NaCl, both of which are of the same order of magnitude as our estimated *k* value. From this fit, it was determined that a 20 hour free corrosion achieved approximately 50% and 10% of the saturation value, C_s, for Mg and Al, respectively (Figure 3.24.b).

Once accurate fits for the first-order rate expression were obtained, average dissolution rates for Mg^{2+} and Al^{3+} per surface site were determined using Equation 16,

$$N_D = \frac{C N_A V}{t\, n} \tag{3.17}$$

Where, N_D is the dissolution rate per site ($atoms\ s^{-1} site^{-1}$), *C* is the ion concentration ($mol\ L^{-1}$), N_A is Avogadro's number ($N_A = 6.022 * 10^{23}\ atoms\ mol^{-1}$), *V* is the total volume of electrolyte (V = 0.002 L), *t* is the time (*s*), and *n* is the number of lattice sites

on the exposed area. The number of exposed lattice sites was estimated assuming that the basal (0001) plane was most prevalent for Mg and the close packed (111) plane was most prevalent for Al. For an exposed area of 0.124 cm^2, the number of sites was estimated to be 1.39×10^{14} for Mg and 8.73×10^{13} for Al. Using the experimental dissolution data (Fig. 10a) the average dissolution rate was determined to be 0.222 and 0.022 ions s^{-1} $site^{-1}$ for Mg^{2+} and Al^{3+}, respectively.

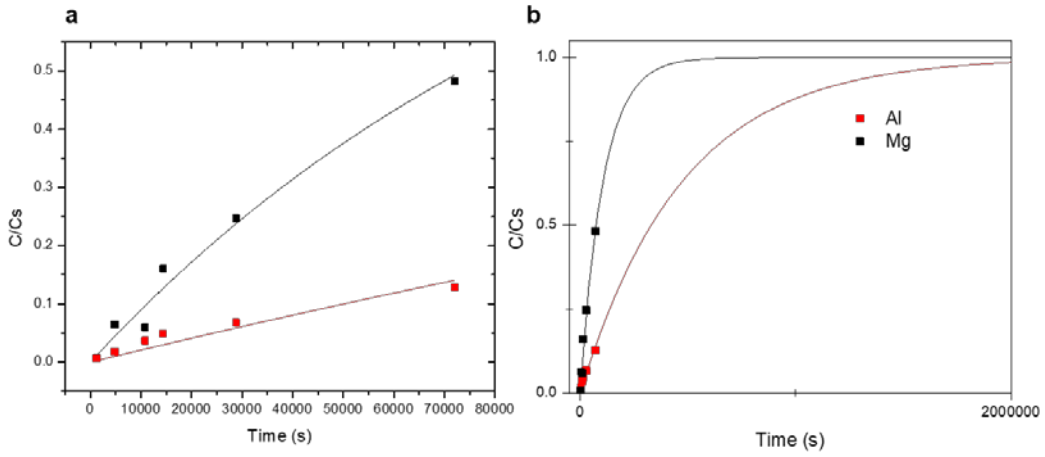

Figure 3.24. First-order rate expression for Mg and Al dissolution in 3.5% NaCl where (a) shows the fitted exponential equation during a 20 hour free corrosion where Mg (black) $k_{Mg} = 9.419 \times 10^{-6}$ and Al (red) $k_{Al} = 2.103 \times 10^{-6}$ and (b) shows the fitted exponential equation until the solution reaches saturation.

3.4.5. Ionic Liquid Dissolution

Dissolution potential of commercial alloys, binary-phase alloys, and component phases.— In an effort to minimize the various side reactions that occur during Mg

dissolution in aqueous conditions, dissolution studies of Mg and Mg-Al alloys were performed in absence of water using CC-Urea ionic liquid electrolyte. LSV was used to assess the anodic behavior of binary-phase alloys, commercial alloys, and component phases, the results of which are summarized in Figure 3.25. Al exhibited strong passivity in the tested potential window while the dissolution potentials of Mg and binary-phase alloys ranged from -600 mV to 200 mV (vs. Al^{3+}/Al), suggesting targeted Mg attack. The peak current density of all alloys was higher than that of CP Mg, with the exception of AM60. Of the tested alloys, Mg-8%Al and all three commercial alloys display dissolution potentials less noble than CP Mg. Two dissolution peaks are observed for alloys containing secondary phases (Mg-8at.%Al and commercial alloys). Although the locations and sharpness of the peaks vary, it is possible that they are related to preferential phase dissolution.

Morphology studies of binary-phase alloys.—The morphology of commercial alloys (Figure 3.26) and single-phase binary alloys (Figures 3.27-28) following 60 minute potentiostatic dissolution in 150°C ChCl-Urea ionic liquid was observed using SEM. As seen in Figure 2.26.a-b., AZ91D displays a highly regular mesh-like morphology composed of ridges surrounding 5 μm diameter pits, accompanied by significant Al surface enrichment up to approximately 40 at.% Al (Figure 2.26.c). Alloys containing lower concentrations of Al display more irregular morphologies with ridge-like and platelet-like structures located on the substrate.

Both single-phase alloys form highly ordered surface morphologies following 60 minute potentiostatic dissolution in 150°C ChCl-Urea. Dissolution potentials of -600 mV and -100 mV (vs. Al^{3+}/Al) were chosen for α-Mg-2%Al and α-Mg-5%Al, respectively, based on the LSV behavior of each alloy in the electrolyte (Figure 3.25a).

As seen in Figure 3.27, α-Mg-5%Al produces an ordered, mesh-like morphology composed of ridges surrounding pits of approximately 10 μm diameter. This is significantly smaller than the 500 μm grain size observed in the alloy. Higher magnification reveals these ridges to be composed of Al-nanowires (Figure 3.27.b-c). The pits, meanwhile, contain high levels of Mg true to the original substrate composition. SEM characterization of α-Mg-2%Al, meanwhile, reveals the development of a cracked surface morphology composed of Al-rich platelets, shown in Figure 3.28. This is similar to the surface morphology evolution of αMg-2 at.% Al during 20h free corrosion at 1600 rpm in 3.5% NaCl, and a side-by-side comparison is provided in Figure 3.29.

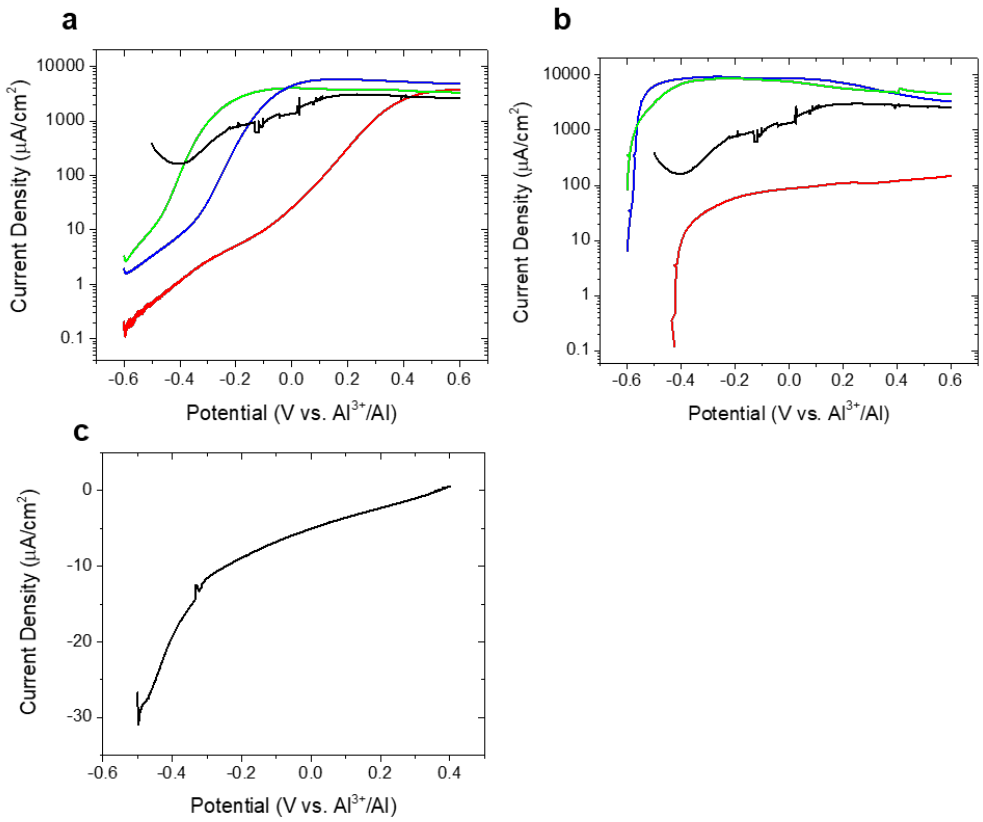

Figure 3.25. Anodic dissolution waves for synthetic alloys and component phases. LSV was performed in 150°C ChCl-Urea using 99.999% Al wire reference, Pt mesh counter electrode from lower limit -0.6 V to upper limit 0.6 V (vs. Al^{3+}/Al) at 10 mV/s. Figure (a) shows results for 99.95% Mg (black), αMg-2%Al (blue), αMg-5%Al (red), and Mg-8%Al (green). Figure (b) shows results for 99.95% Mg (black), AZ31B (blue), AM60 (red), and AZ91D (green). Figure (c) shows results for 99.999% Al.

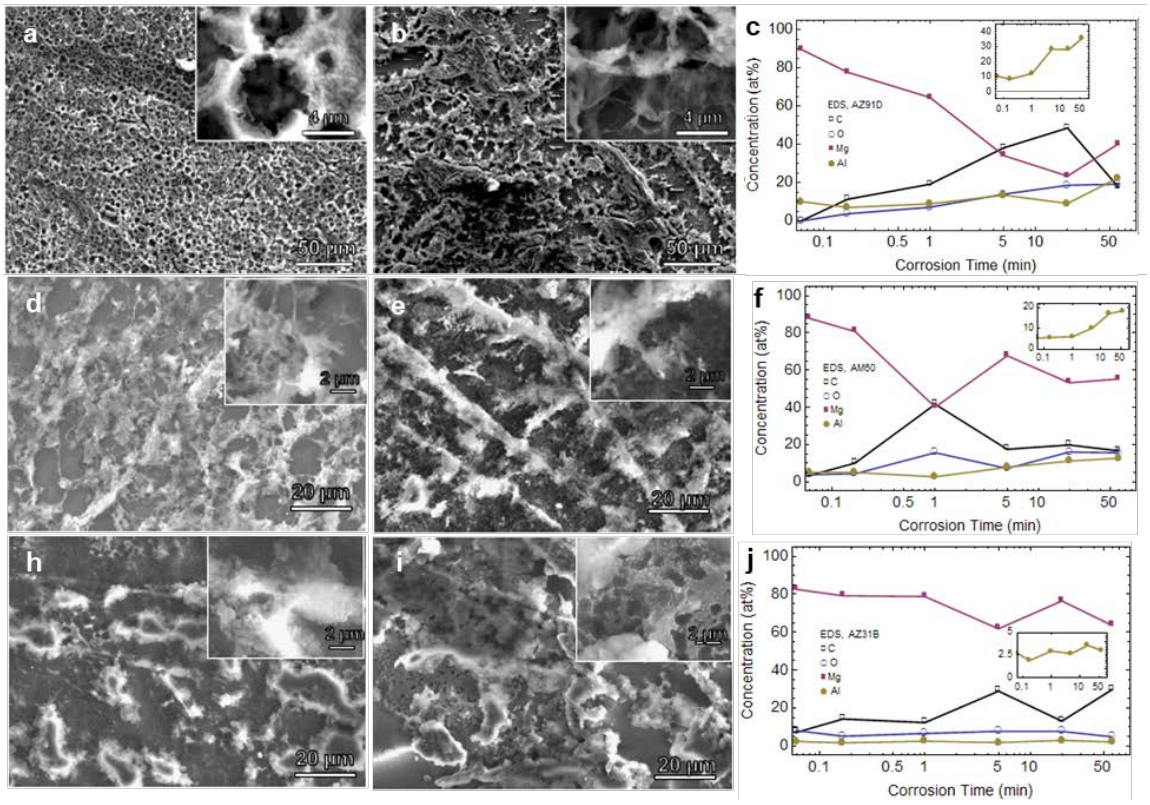

Figure 3.26. SEM images of commercial alloy surface morphologies following potentiostatic dissolution in ChCl-Urea for the indicated times at -220 mV vs. Top panel: AZ91D, for a) 20 minutes, b) 60 minutes; Middle panel: AM60, d) 20 minutes, e) 60 minutes; Bottom panel AZ31B, h) 20 minutes, i) 60 minutes. The corresponding insets show higher magnification images. Plots c), f), and j) are the corresponding EDS compositional data. These insets show the Al concentration normalized to Al+Mg.

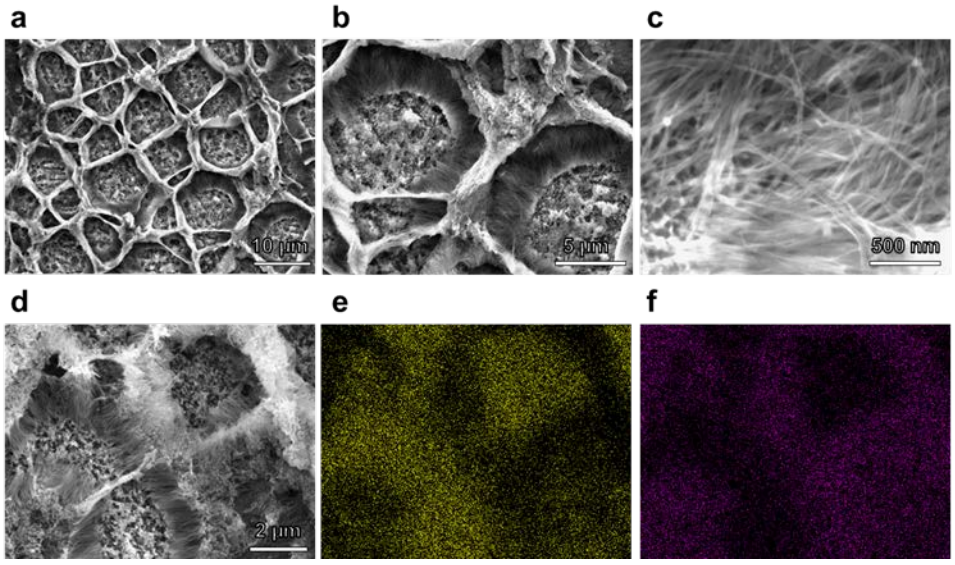

Figure 3.27. Surface morphology using SEM of α Mg-5at% Al following potentiostatic corrosion at -100 mV vs. Al/Al^{3+} for 60 min in a deep eutectic 1:2 molar ratio of choline chloride:urea at 150 °C shown at increasing magnification (a-c) as well as EDS areal mapping of the base, nanowire and ridge morphology shown in d) for e) Mg and f) Al abundance.

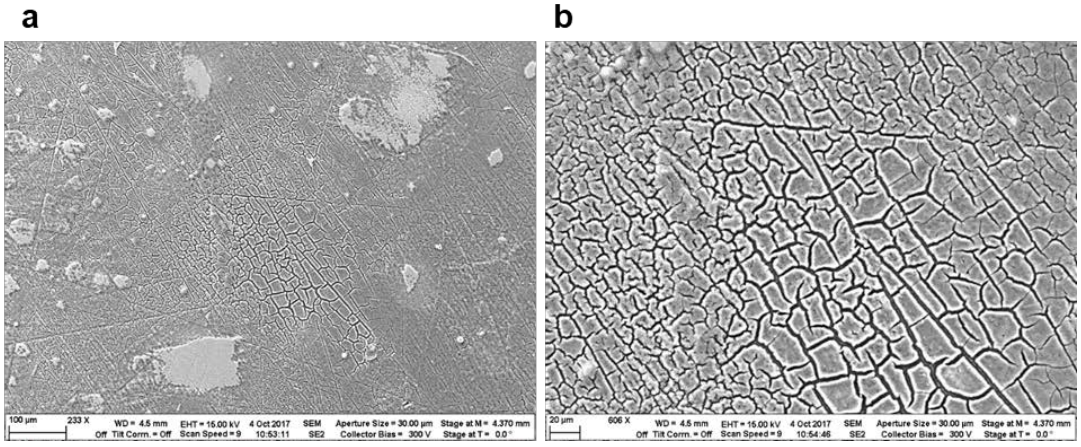

Figure 3.28. Surface morphology of αMg-2 at% Al potentiostatically held at -600 mV vs. Al/Al^{3+} for 60 min in CC-urea at 150°C shown at increasing magnification.

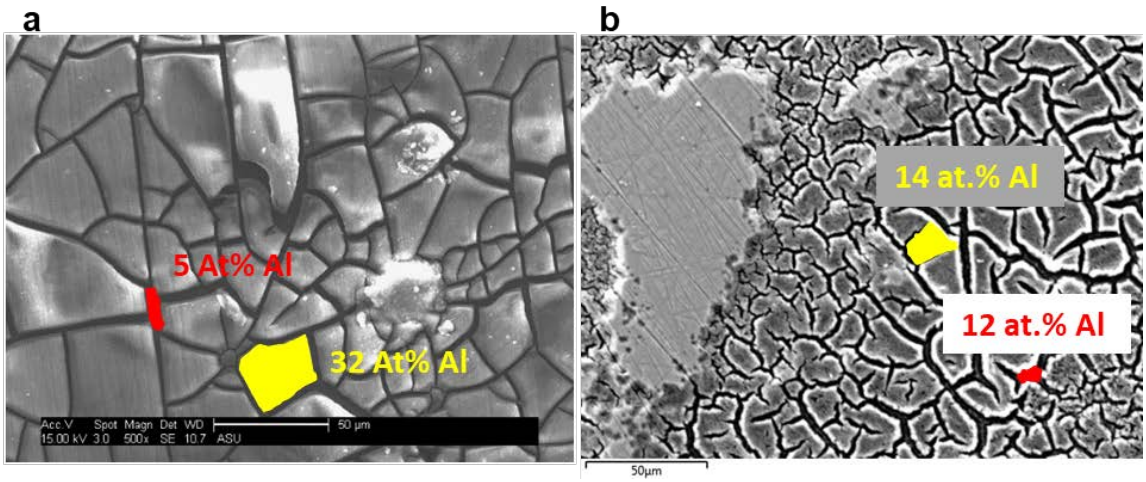

Figure 3.29. Surface morphology using SEM of αMg-2 at% Al. Left: 20h corrosion at 1600 rpm in aqueous chloride. Right: potentiostatically held at -600mV vs. Al wire for 60 min in CC-urea at 150C.

3.5. Conclusions

Both aqueous free corrosion and ionic liquid dissolution studies indicate surface enrichment of Al during the corrosion process. In the case of polarization experiments, shifts in the corrosion potential indicate changes in surface composition. Nearly all alloys display positive corrosion potential shifts over time during free immersion in aqueous chloride. Polarization studies also revealed pitting potentials for all three binary-component alloys after one minute of free immersion that were no longer present following 20 hour immersion. "Accelerated" free corrosion in single-phase binary alloys revealed the development of an Al-rich platelet surface morphology, which led to up to 26 at% increase in the overall surface concentration of Al. Additional dissolution studies

performed in ionic liquid similarly produced Al-rich surface morphology evolution in single-phase binary Mg-Al alloys.

In both “accelerated” free corrosion and ionic liquid dissolution, α-Mg-2%Al displayed significant surface enrichment of Al in the form of Al-rich platelet formation. Similar platelet formation was observed in α-Mg-5%Al during “accelerated” free corrosion testing. Interestingly, platelets were measured to contain the same Al concentration, seemingly independent of the substrate coverage. Surface coverage of Al-rich structures was significantly higher in α-Mg-2%Al, however, leading to greater overall Al surface concentration.

Studies performed on α-Mg-5%Al revealed very different morphology evolution depending on the experiment type. In the case of aqueous “accelerated” free corrosion, Al-rich platelets very similar to those on the surface of α-Mg-2%Al were observed. For ionic liquid dissolution, however, an Al-rich web morphology was revealed, similar to that displayed in higher Al concentration commercial alloys (i.e. AZ91D). The reason for these large changes in the morphology evolution has yet to be determined, although we speculate that this is at least in part due to surface diffusion during the dissolution process.

Atmospheric studies confirm rapid roughening of sample surfaces and pH 10 stabilization. Additions of Al had a general tendency to slow these processes slightly,

although not significantly. These results allowed us to confirm rapid formation of an unstable pH environment for elemental Al and more accurately measure first-order reaction rate kinetics of Mg an Al dissolution, where $k_{Mg} = 9.419\ x\ 10^{-6}\ s^{-1}$ and $k_{Al} = 2.103\ x\ 10^{-6}\ s^{-1}$.

Despite the evidence of Al enrichment, no passivation was observed in low-Al content binary Mg-Al alloys or commercial alloys. While bulk Al may develop on the surface during the dissolution process, the Al concentration is simply not high enough to allow formation of large enough structures to cover the entirety of the exposed surface area. That said, Al enrichment at the surface may occur by the following description, also shown in Figure 3.30.

Within the solid-solution matrix, Mg is the active component and Al the more noble component. Microgalvanic corrosion acts as the primary corrosion mechanism. Mg will be preferentially dissolved from the surface, and this dissolution will favor sites with fewer nearest neighbors, such as step and kink sites. Al redistribution occurs as Al atoms will diffuse along the surface, collecting at step edges. Since Mg will be preferentially dissolved from the step edge, the Al atoms will move tangentially with the step as it is pushed back along the surface, eventually leading to agglomeration of Al atoms. As the agglomerated structures continue to grow, they begin to act as bulk Al, passivating on the surface in the form of a standalone "island". Due to the low concentration of Al within the α-matrix, these agglomerated structures are unable to form a full coverage passive

film at the surface, and instead act as Al oxide islands that are galvanically coupled with the substrate. These islands serve as cathodic sites, contributing towards the production of a hydroxide layer at the surface and subsequent pH increases. As the pH continues to increase, the Al oxide islands lose stability and dissolve from the surface if they are not first undercut by continued Mg dissolution. In the case of commercial alloys, this process is "accelerated" due to the presence of secondary phases, resulting in larger-scale galvanic corrosion.

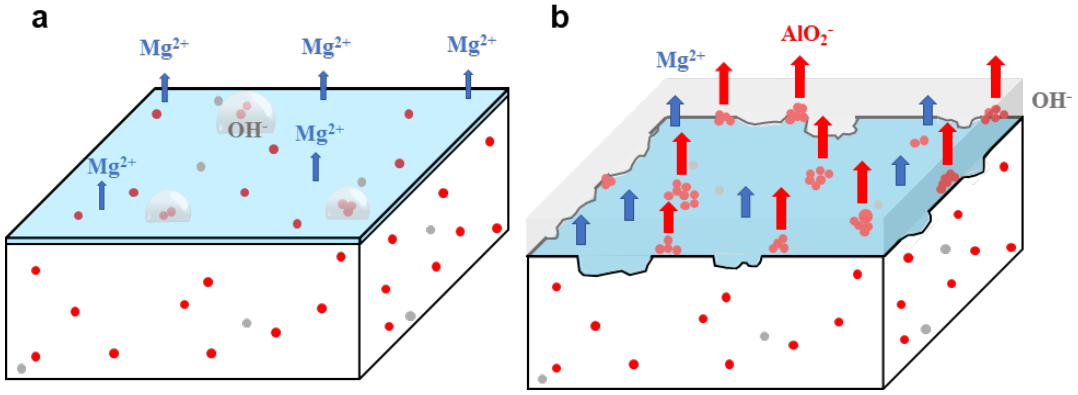

Figure 3.30. Corrosion process in Mg-Al alloys in solid solution. Al atoms (red) and impurity atoms (grey) are present within the Mg matrix (white). A magnesium hydroxide layer (light blue) covers the surface. (a) In near neutral electrolyte, Mg cations dissolve from the surface, resulting in Al enrichment, while Al clusters act as cathodic sites for water reduction, producing localized hydroxide buildup. (b) As Mg continues to dissolve, the surface roughens, and diffusion of hydroxide results in a surface pH 10 environment (light grey). Al is no longer stable in this pH regime and dissolves from the surface in the form of aluminate anions.

Percolation theory can be used to provide a theoretical possibility for the production of a passive surface film in binary, single-phase Mg-Al alloys. Knowing the 3D site percolation threshold, p_{3D}, of the Mg hcp lattice to be 0.2 [74], this percolation threshold

can be used to estimate the required concentration for formation of a fully connected Al structure across the surface, allowing for passivation. This would cause us to assume that, at concentrations below 20 at.% Al, full percolation of Al across the surface will not occur, allowing for undercutting of any areas of bulk Al at the surface. As such, no passivation is likely in Mg-Al alloys containing less than 20 at.% Al. In studies of AZ91D alloys performed by Ambat et. al., preferential dissolution of areas containing less than 8 wt% Al within the α-phase Mg-Al matrix is observed [61]. Were higher Al concentrations to be distributed in the α-matrix, passivity may be achievable.

Due to the fact that the solubility of Al in solid solution is 11.6 at.% [8], a third component will likely be required to stabilize higher concentrations of Al in solid solution with Mg. Continued work is being done to determine suitable candidates for this purpose using our experimentally-derived rate kinetics for dissolution rates of Mg and Al.

4 Ni-Cr Alloys

4.1. Introduction

Stainless steel is a well-studied system known for its passivity in most dilute, aerated solutions. This passive behavior is typically attributed to chromium compositions at or above 12-13 at.%, although the exact details of this process are still not well understood. Below this threshold composition, the alloy does not display passive behavior. Although pure chromium is more electrochemically active (more negative standard potential) than both nickel and iron, chromium acts as the “more noble” component since it passivates at lower potentials than the standard potentials of both nickel and iron via atmospheric formation of a highly stable chromium oxide layer. While chromium’s brittle nature and resistance to fabrication techniques make elemental applications unappealing for industrial purposes, this ability to easily form a very stable, thin, resistant surface film makes chromium ideal for alloying purposes [14].

Our interest lies in single-phase, binary alloys, as it serves as the simplest case for studying micro-galvanic aqueous corrosion processes. Of the binary systems composing stainless steels, Fe-Cr has been studied extensively, with significantly less research being performed on the Ni-Cr system. Both systems display stainless-like passivity with additions of 12-13 at.% Cr. Ni is less electrochemically active (more positive standard potential) when compared with Fe, however, and it is well known for its low corrosion

rates in acid solutions, with Cr additions inducing passivation and corrosion resistance, even in the presence of oxidizing solutions [14]. Additionally, within the composition range of interest (0-25 at.% Cr), Ni displays full solubility in solid solution with Cr, whereas Fe passes through four different phase regions. This led to our focus on the Ni-Cr system to study passivity in solid-solution binary-component alloys. By studying the corrosion behavior of the ideally passive Ni-Cr system, it may be possible to shed some light on aqueous corrosion mechanisms and compositional-dependent passivity in single-phase alloys, providing insights for design of new stainless-like alloys.

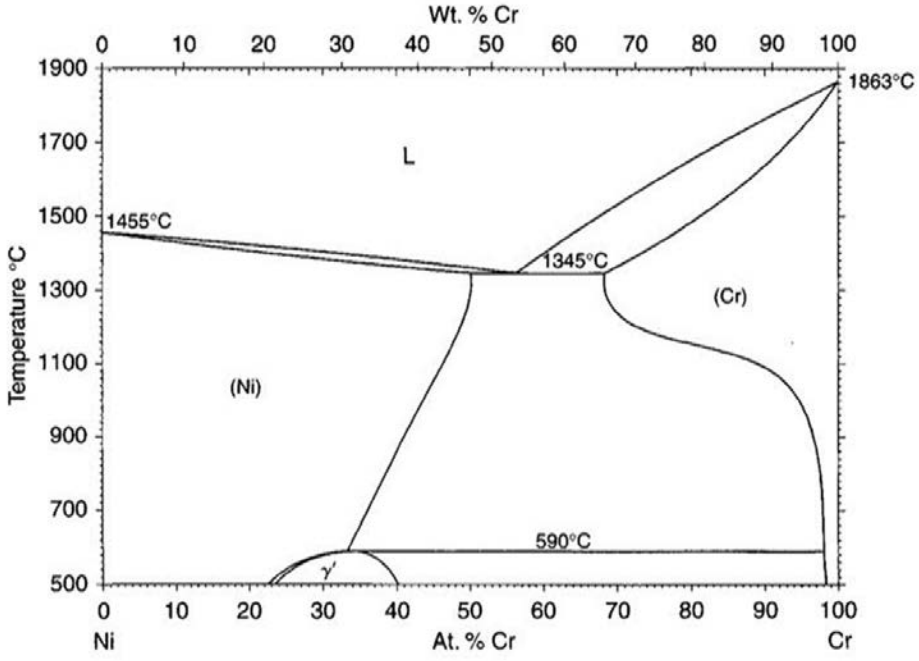

Figure 4.1. Ni-Cr phase diagram [75].

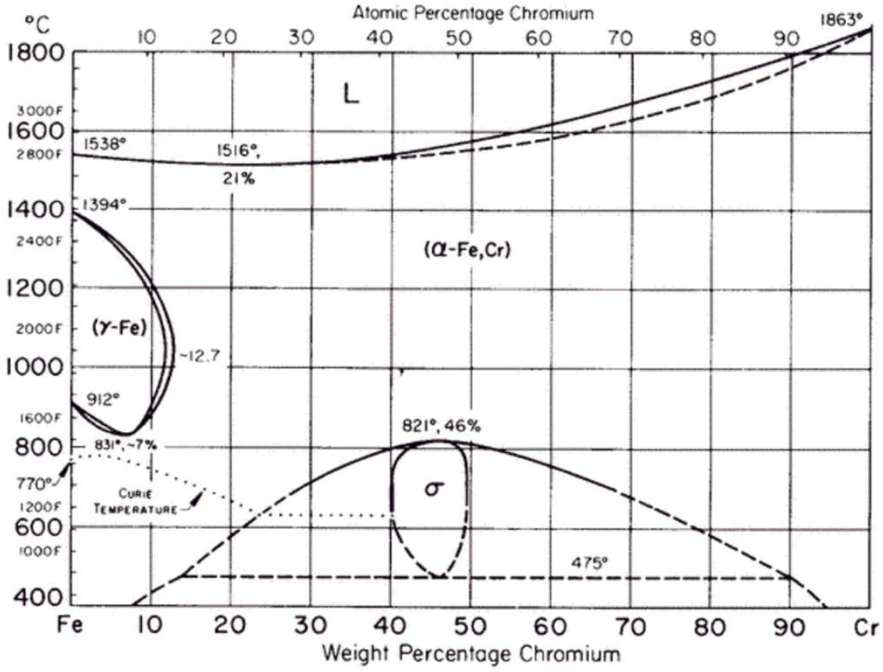

Figure 4.2 Fe-Cr phase diagram [76].

4.2. Background

4.2.1. Passive Film Formation

Although electrochemical studies of the Ni-Cr system is limited, film formation studies have been performed on Ni-Cr alloys using transmission electron microscopy (TEM) and scanning tunneling microscopy (STM). It is generally understood that a primary crystalline passive film will form on the surface of Ni-Cr alloys which, unlike passive films in the Fr-Cr system, will maintain long-range crystallinity independent of time or Cr concentration [10],[77]. The mechanism behind the formation of these films on a

micro-scale is still uncertain. Luo observed film formation via a nucleation and growth process at elevated temperatures of 700°C using in-situ TEM [77]. Island formation begins with the nucleation of NiO islands, which grow to form a thin film composed of NiO and Cr_2O_3 oxide phases. In the case of alloys with Cr concentration less than 12 at.%, the film will eventually stabilize into a two-phase system composed of primary oxide and secondary oxide. The primary oxide is composed of large, densely packed $NiCr_2O_4$ islands while the secondary oxide displays a whisker-like morphology composed of NiO. The secondary oxide acts as a bridge between islands of primary oxide. In the case of alloys with higher Cr concentration, however, a continuous film of $NiCr_2O_4$ will form. TEM imaging of cross-sections of the oxidized layer from Luo reveal thin layers of Cr_2O_3 beneath the NiO islands, lending some doubt as to the formation order of these components [77]. Room temperature controlled oxygen exposure studies on the passive layer of Ni-23 at.% Cr using X-ray photoelectron spectroscopy (XPS) revealed preferential oxidation of Cr within the first 10 L of exposure [78]. Jeng has also suggested the formation of a thin layer of Cr_2O_3 on the substrate surface due to initial absorption of oxygen anions onto Cr surface sites, followed by formation of a secondary layer composed of a combination of Ni and Cr oxides [78]. Ex-situ STM studies performed by Nanjo et. al. similarly reported the formation of a nanocrystalline passive film, with the additional observation that the film grain size decreased with increasing Cr concentration [10]. Thus, while it is generally accepted that a stable passive film forms on the Ni-Cr surface, there is no clear understanding behind the formation mechanism.

Electrochemical testing has been used quite extensively to study film formation in Fe-Cr alloys. Research performed by Frankenthal has revealed two primary stages of film formation that occur during the passivation process of Fe-24at.%Cr in dilute acid solutions [79]–[81]. The first film is formed during the primary passivation process. Frankenthal states that this is a reversible process that occurs within a few millivolts of the primary activation potential where the thin primary passivation film is formed, however we know the surface is dissolving during the active dissolution and primary passivation regimes (Figure 4.3.). This dissolution behavior results in compositional changes at the surface, making any passive film formation an irreversible process. Frankenthal characterizes this reversible film by a thickness corresponding to the adsorption of less than one full monolayer of oxygen anions on the alloy surface. At higher potentials within the passive regime, a secondary passivation process occurs where a secondary film grows to thicknesses exceeding 10 Å. This process is irreversible, as the secondary film grows increasingly stable and resistant to reduction with increasing potential and time. The degree of crystallinity in these films is likely dependent on Cr concentration and time at the passivation potential. Ex-situ scanning tunneling microscopy (STM) studies performed by Ryan et.al. have reported increasing crystallinity with lower Cr concentration [82]. At Cr concentrations of 15 at.%, passive films maintain continuous crystallinity with long-range order while alloys with intermediate concentrations (18-21 at.%) Cr displayed initial short-range order with increased long-range order with atmospheric aging. Higher concentrations of 25 at.% Cr, meanwhile, formed normally disordered five- or seven-membered ring network passive films. While

it is proposed that the time-dependent change in ordering for 18-21 at.% Cr alloys is due to structural relaxation, no clear mechanism has been defined.

4.2.2. Electrochemical behavior

Analytical electrochemical studies on binary systems composing stainless steels have been performed on Fe-xCr alloys[79]–[81],[83], Fe-xNi alloys [84], and Ni-xCr alloys [10]–[12], revealing similar anodic behavior in acidic solutions. As depicted in Figure 4.3, the typical anodic behavior of Fe-Cr and Ni-Cr can be characterized using four primary regimes: (1) active dissolution, (2), primary passivation, (3) passive, and (4) transpassive. The active dissolution regime occurs between the corrosion potential and passivation potential. As the overpotential is increased from the corrosion potential, nickel dissolution from the surface occurs as the oxidation reaction is driven forward. The dissolution rate increases as a function of increasing overpotential, as reflected by the rapidly increasing current density. As nickel continues to dissolve, chromium surface enrichment will occur, along with subsequent Cr-O-Cr network formation. As the surface concentration of chromium increases, the surface will begin to passivate, and the current density will no longer increase, marking the beginning of the second regime—the primary passivation regime. This peak current density occurs at the passivation potential and is referred to as the critical current density. In the passivation regime, the current density will continue to decrease as the passive layer is formed, until finally a stable passivation current density is observed. The potential window of the passivation current

density characterizes the passive regime, where the stability of the passive film prevents further surface dissolution. At high enough potentials, the passive film will no longer remain stable, and surface dissolution will begin again via dielectric breakdown. This is marked by another rapid increase in the current density, which occurs at the transpassive potential.

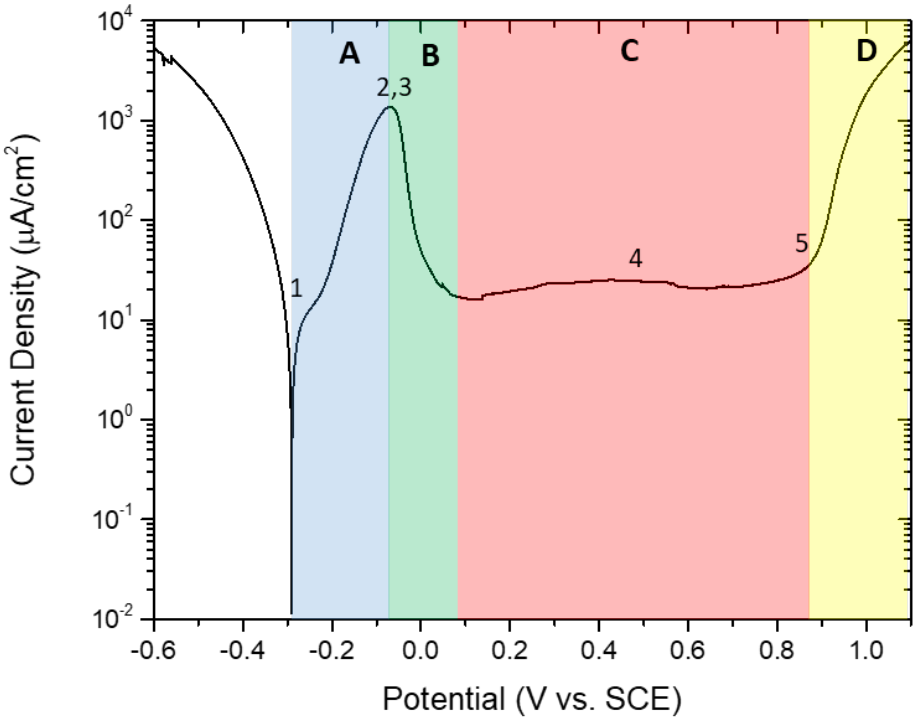

Figure 4.3. The four primary regimes marking general polarization behavior of Ni-Cr alloys: (A) active dissolution, (B) primary passivation, (C) passive, and (D) transpassive. Critical parameters include (1) corrosion potential (E_{corr}), (2) passivation potential (E_p), (3) critical current density (i_c), (4) passivation current density (i_p), and (5) transpassive potential (E_t).

Polarization curves detailing the behavior of Ni-Cr alloys in sulfuric acid solution have been produced by Nanjo and Myers, and additional anodic data has been reported by

Bond in the form of critical current densities and passivation potentials. Of the reported polarization curves, only Nanjo examines alloys near the Cr concentration of interest—12 at.%. All three groups report decreasing current density and passivation potential as a function of increasing Cr concentration. Bond also went on to report that the presence of oxygen and concentration of sulfuric acid affect polarization behavior and corrosion rate of Ni-xCr alloys [12]. These effects were not studied independently since Bond did not study the effects of sulfuric acid concentration in absence of oxygen. Of the three groups, only Myers reports polarization results for alloys with Cr composition ranging from 0-100%. While Myers observes lower critical current density and lower passivation potential with increasing Cr concentration for low Cr content alloys below 25 at.% Cr, he observes a change in this trend for mid-Cr concentrations ranging from 25 at.% to 95 at.% Cr where the passivation potential remains relatively constant while the critical current density continues to decrease. High-Cr concentrations exceeding 95 at.% Cr reveal a sudden, sharp decrease in passivation potential, accompanied by simultaneous increase in the critical current density. Neither Nanjo or Myers report any appreciable concentration dependence in the onset of the transpassive regime, with both groups reporting this to occur at approximately 900 mV (vs. SCE) in dilute deaerated sulfuric acid solutions [10],[11].

4.2.3 Percolation Theory

A possible explanation for this critical composition is described by the percolation model, developed by Sieradzki and Newman, where passivity is achieved in the presence of the infinite cluster of Cr [85]–[88]. In the case of a simple, 2-D lattice, the infinite cluster is defined by a percolating network of occupied sites, in this case Cr atoms, that reaches both ends of the lattice in both the x- and y-directions. An example of an infinite cluster involving 1st and 2nd nearest neighbors (nn) for a 2-D surface is presented in Figure 4.4. Since passivity is defined by the formation of a thin, passive film at the surface, the defining characteristics of the infinite cluster do not change significantly even in the 3-D lattice. In three dimensions, the infinite cluster still must extend to either side of the lattice in both the x and y directions. No realistic surface will be perfectly atomically flat, however, which is the scenario presented in the 2-D case. Instead, we must account for the roughened surface that is produced when the passive film forms over an actively dissolving surface. We now consider filled sites that percolate in the z-direction, in addition to those connected in the x- and y-directions, as contributors towards the infinite cluster. A simplified example of this is provided in Figure 4.5., where we see that the infinite cluster now resembles a roughened surface, similar to what may be produced during the corrosion process.

When examining site percolation probability, a sharp threshold is observed at a critical concentration (p_c), also referred to as the percolation threshold, representing the

concentration of occupied sites (or bonds) at which the infinite cluster will appear. Below the critical degree of percolation, the infinite cluster will not appear since not enough percolating sites exist to fulfill the necessary requirements to form the infinite cluster. While continuous structures may form at small length scales, they do not extend from one edge of the surface to the other and are susceptible to undercutting as the surface is actively dissolving during the corrosion process. Once a sufficient number of sites have been filled, however, the infinite cluster appears. The probability of observing the infinite cluster will continue to increase with increasing concentration. In this case, the occurrence of percolation is defined by the Cr concentration. From the well-known behavior of stainless steels, one may be likely to guess the percolation threshold to be 0.12-0.13.

A more careful estimation of the percolation threshold can be made by considering the crystal structure of the bulk alloy and chemical composition of the passive film. The Ni-Cr lattice forms an FCC crystal structure. The passive film is formed by adsorption of oxygen anions onto the surface, which form Cr-O-Cr bonds that subsequently create the passive oxide film composed of Cr_2O_3. To achieve this, chromium atoms must be situated in close enough proximity to one another to be bridged by O bonds on the sample surface. Using the hard ionic sphere radii of O^{2-} (1.4 Å) and Cr^{3+} (0.62 Å), the maximum distance between Cr atoms at the surface can be estimated to be 4.40 Å. For the FCC Ni-Cr lattice structure with an approximate lattice parameter of 3.55 Å, this means that Cr atoms must be first or second nearest neighbors to contribute towards the formation of a

continuous Cr-O-Cr network across the sample surface. For first and second nearest neighbors in the FCC lattice, the 3D site percolation threshold, p_c^{3D}, is equal to 0.137.

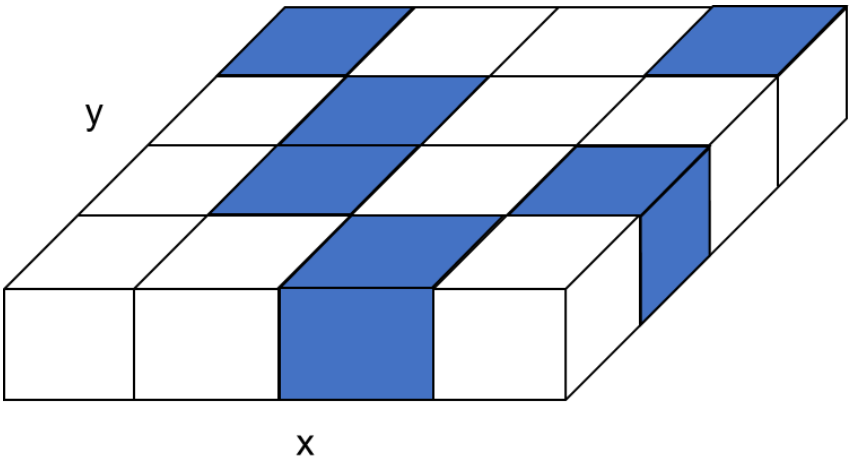

Figure 4.4. The infinite cluster for 1st and 2nd nn for a flat 2-D surface. Cr atoms are represented by blue sites and Ni atoms are represented by white sites. The Cr atoms form a percolating network across the surface in both the x and y directions.

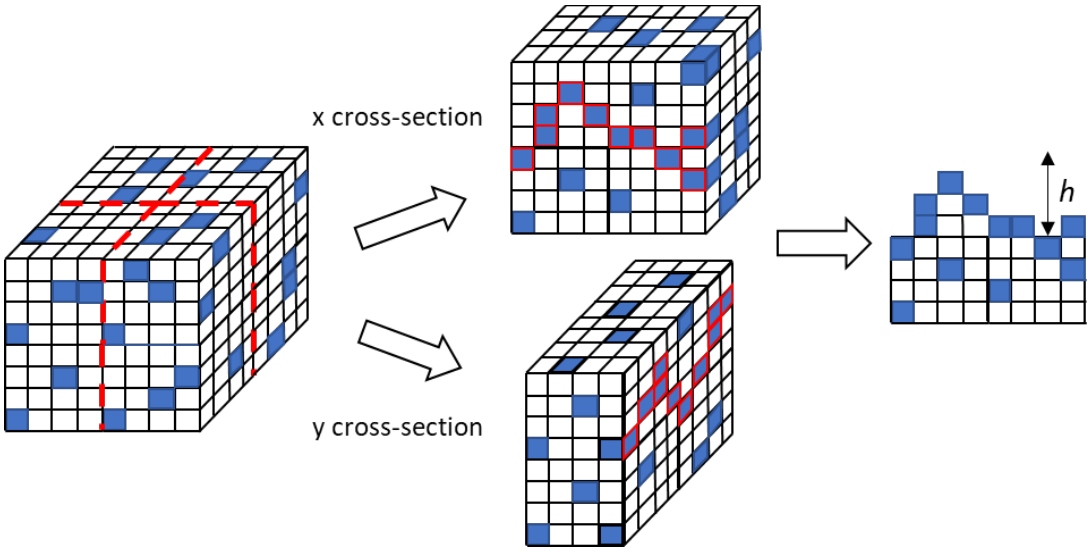

Figure 4.5. Simplified illustration of the infinite cluster in a 3D lattice. Cross-sections in the x and y directions reveal examples of what the infinite cluster (outlined in red) may look like in each direction for 1st and 2nd nn. On the far right, the layers above the "x cross-section" infinite cluster in the z-direction have been removed to better show the idea of the roughened surface passive film. The number of dissolved monolayers, *h*, is defined by the deepest penetration in the z-direction.

Sotta and Long have performed extensive research exploring the theoretical connections between 2D and 3D percolation [89]. For a finite size film of with thickness *h*, the percolation threshold is described by Equation 4.1.:

$$p_c(h) = p_c^{3D} + c\, h^{-1/\nu^{3D}} \tag{4.1.}$$

where p_c is the percolation threshold, p_c^{3D} is the 3D percolation threshold (0.137 in the case of the FCC lattice), c is a dimensionless prefactor, h is the film thickness (number of monolayers), and ν^{3D} is the 3D critical exponent for the correlation length (0.878). In the case of Ni-Cr, the film thickness, *h*, is equivalent to the dissolved number of monolayers,

defined by deepest penetration in the z-direction (Fig. 4.5.). If we think of the infinite cluster as the passive film, we assume all layers between the surface and the infinite cluster will be dissolved due to preferential dissolution of the more active component and undercutting of the more “noble” component. We assume all layers below the infinite cluster will not dissolve since they are protected by a passive film.

In an effort to test these percolation ideas in the “ideal” Ni-Cr system, Ni-Cr alloys of variable Cr concentration near the critical composition have been electrochemically observed. Polarization studies have been used to define the passivity behavior as a function of composition. Potential pulse experiments were also used observe time-dependent passivity as a function of composition, including passivation current density and monolayer dissolution. Experimentally measured monolayer dissolution could then be compared with predicted behavior with percolation theory.

4.3. Methods

4.3.1. Alloy characterization and preparation

Ni-Cr compositions ranging from 5-25 at.% Cr were examined. A total of 9 compositions were examined: 5.2, 8.2, 9.9, 11.7, 14.9, 16.6, 20.1, 23.1, and 24.1 at.% Cr. EDS was used to confirm the sample compositions. Discs of 1mm thickness and 20mm diameter were cut using EDM. Each disc was then polished up to 4000p using silicon carbide

paper and ethanol lubricant, followed by ethanol rinse. To ensure solid solution, a 27 hour heat treatment was executed in inert gas environment. Samples were heated to 1100°C for 24 hours, then left at 800°C for 3 hours, followed by a RT water quench.

4.3.2. Experimental setup

All aqueous testing was performed in a 30 mL Teflon beaker with an 8.5mm diameter opening in the bottom. Samples were secured beneath this bottom opening using an O-ring inserted between the sample surface and Teflon cell. To effectively seal the O-ring, a stainless steel plate was placed beneath the sample and screwed into the bottom of the Teflon cell. Electrochemical experiments were then performed in deaerated 0.1M H_2SO_4 using Pt mesh counter electrode and SCE reference electrode.

4.3.3. Passivation Characterization

No additional sample preparation was performed on the surface prior to passivation characterization. To reduce the surface oxide layer, a 30 minute cathodic hold was performed at -1.5 V vs. SCE. A linear sweep was then initiated from lower potential limit -0.6 V vs SCE to upper potential limit 1.1 V vs SCE at 1 mV/s.

4.3.4. Passivation Potential Pulse

Samples were polished up to 4000p using silicon carbide paper and ethanol lubricant. After loading in the Teflon cell described above, a 30 minute cathodic hold was performed at -1.5 V vs. SCE to reduce the surface oxide layer. The potential was then held at 0.6 V vs. SCE until a stable current was observed, typically for 20 minutes. The passivation current density was obtained using the stable current, and the surface charge density was calculated by integrating the area under the CA curve, using the passivation current as a baseline.

4.4 Results and Discussion

4.4.1. Polarization Observation of Passivation Behavior

The polarization behavior data for all Ni-Cr concentrations is summarized in Figure 4.6. While the Cr composition has no observable effect on the corrosion and transpassive potentials, the passivation potential, passivation current density, and critical current density decrease as a function of increasing Cr composition. These observations confirm the trends observed by Bond, Nanjo, and Myers in previous polarization studies performed on Ni-Cr alloys [10]–[12]. More detailed passivation potential and critical current density values as a function of composition are provided in Figure 4.7. Both the passivation potential and critical current density display decay with increasing Cr

concentration. Consistent with reports by Myers, the majority of rapid decay occurs at low Cr concentration, below 12 at.%, with the alloy displaying more Ni-like behavior. At mid-level ranges between 12 and 25 at.% Cr, the rate of decay decreases, the passive window is extended, and the alloy displays more Cr-like behavior.

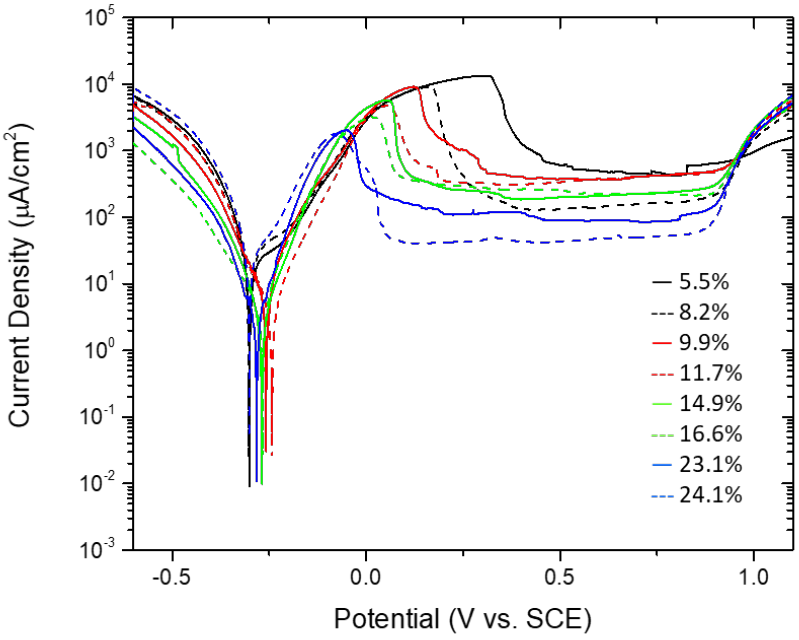

Figure 4.6. Linear sweep voltammetry for Ni-x at.%Cr alloys in deaerated 0.1M H_2SO_4 from V_L = -0.6 V (vs. SCE) to V_U = 1.0 V (vs. SCE) at sweep rate 1 mV/s using SCE reference electrode and Pt mesh counter electrode.

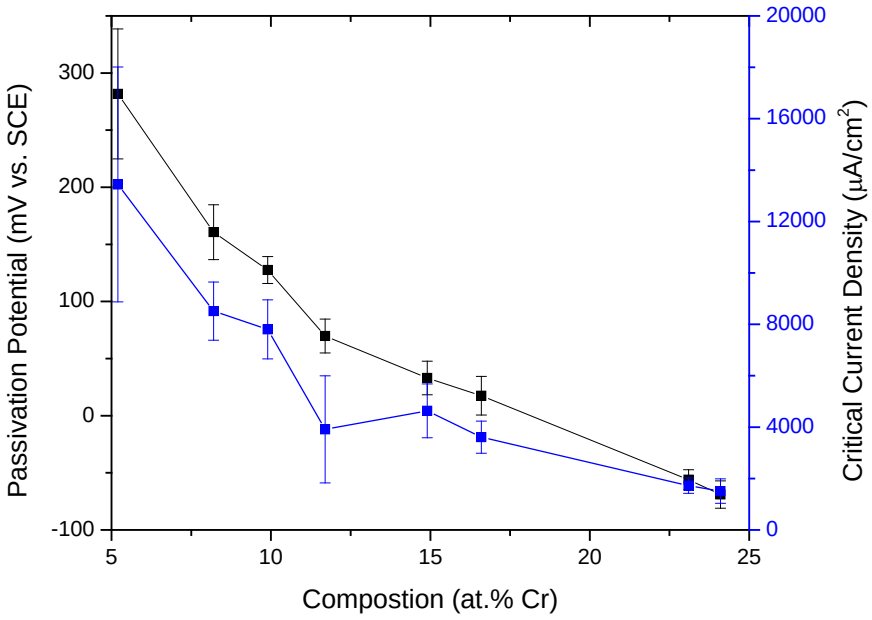

Figure 4.7. Passivation potential (black) and critical current density (blue) as a function of at.% Cr composition in binary Ni-Cr alloys in deaerated 0.1M H_2SO_4 . Error bars indicate standard deviation of the average value for four samples of each composition.

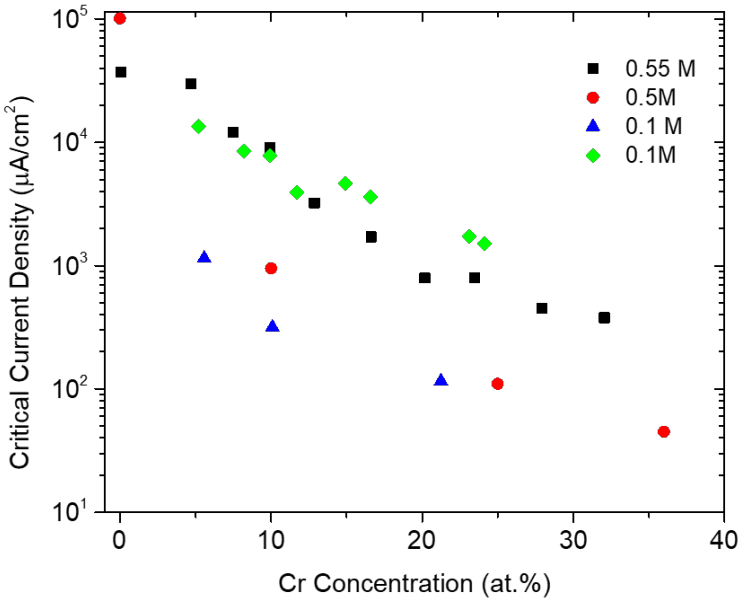

Figure 4.8. Critical current density of Ni-xCr alloys in variable concentration deaerated sulfuric acid solution as a function of Cr composition. Experimental data is shown in green, along with data from Bond (0.55 M, black) [12], Myers (0.5 M, red) [11], and Nanjo (0.1 M, blue) [10].

To assess whether the experimental data was in good agreement with the literature, our critical current density data has been overlayed with previously reported data sets within the relevant Cr concentration range (0-40 at.% Cr) in Figure 4.8. It is worth mentioning that each of the three literature-obtained data sets use a different concentration of H_2SO_4 as the electrolyte, with Myers additionally adding 0.25 M K_2SO_4 to his 0.5M H_2SO_4 electrolyte to increase the electrolyte conductivity [11]. The experimental data was performed in the same concentration as that used by Nanjo—0.1 M H_2SO_4—in an effort to obtain a close comparison with at least one set of previously reported values. Although the experimental values are approximately one order of magnitude higher than

those reported by Nanjo in the same electrolyte concentration, the data fits well with literature values as a whole.

As expected, the window of the passive regime is extended as the Cr concentration increases. Passive-like behavior is still observed in low-Cr content alloys, below 12 at.%, which may appear to contradict the idea of percolation theory. Nickel displays quasi-passive behavior in dilute sulfuric acids, however, due to saturation and subsequent precipitation of salt surface films. This salt film formation has been observed in both pure iron [90] and nickel [91] in sulfuric acid environment.

4.4.2. Monolayer Dissolution Using Potential Pulse

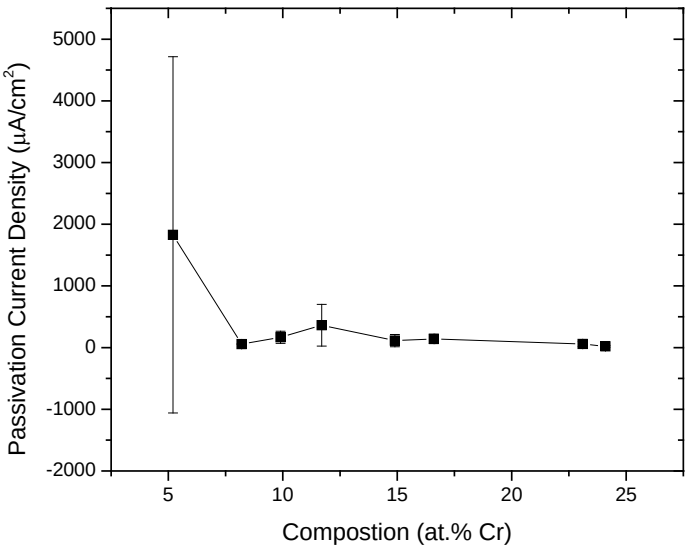

Figure 4.9. Passivation current density of Ni-xCr alloys in 0.1M deaerated sulfuric acid solution as a function of Cr composition. Data collected using passivation potential pulse from -1.5V to 0.6V vs. SCE.

While LSV provides valuable polarization data, this method can prove challenging when time-dependent mechanisms are being observed. As such, potential pulse studies were used to more accurately measure more time-dependent aspects of the passivation process, including the passivation current density and monolayer dissolution. Passivation current densities were observed by allowing the current density to stabilize while holding a constant potential within the passive regime. As shown in Figure 4.9., the passivation current density has a tendency to decrease with increasing Cr composition. By integrating the chronoamperometry curve, the surface charge density required for passivation as a function of Cr composition could be measured, the results of which are summarized in Figure 4.10. It is important to note that the background passivation current density was subtracted prior to evaluating the surface charge density.

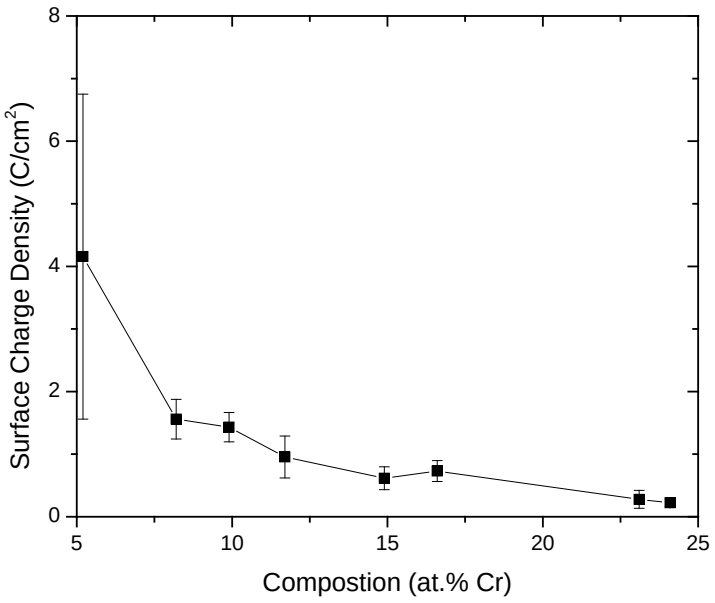

Figure 4.10. Surface charge density of Ni-xCr alloys in 0.1M deaerated sulfuric acid solution as a function of Cr composition. Data collected using passivation potential pulse from -1.5V to 0.6V vs. SCE. Error bars indicate standard deviation of four samples.

4.4.3. Experimental Comparison with Percolation Theory Predictions

We compared our experimental results to the theoretical values predicted by percolation theory by converting the measured surface charge density to average number of monolayers dissolved. First, the surface charge density per monolayer was calculated for the FCC (111) plane for first nearest neighbors, $\frac{\sqrt{2}}{2}a$. The surface atom density, *n*, was calculated using Equation 4.2.:

$$n = \frac{N_{111}}{A_{111}} = \frac{3\left(\frac{1}{6}\right)}{\frac{1}{2}\left(\frac{\sqrt{2}}{2}a\right)\left(\frac{\sqrt{6}}{4}a\right)} = \frac{0.5}{\frac{\sqrt{3}}{8}a^2} \quad (4.2.)$$

where N_{111} is the number of atoms A_{111} is the surface area (cm^2), and a is the lattice parameter (cm). The lattice parameter of FCC Ni-Cr alloys has been reported as a function of composition using a series of experimental and calculated data sets by Wu, et al [92]. This was used to determine the lattice parameter for each tested composition, all of which are listed in Table 4.1. After converting these values to units of mol/cm^2 using Avogadro's number ($6.022 * 10^{23} atoms/mol$), we can calculate the estimated surface charge density for each dissolved monolayer:

$$Q = znF \tag{4.3.}$$

where z is the charge (here we are assuming a charge of +2 for both Cr and Ni dissolution), n is the surface atom density (mol/cm^2), and F is Faraday's constant ($96485\ C/mol$). By dividing the experimentally measured surface charge density by the calculated surface charge density per monolayer (Table 4.1.), the average number of dissolved monolayers can be derived.

Compostion	Lattice Parameter	n	Monolayer Charge Density
at.% Cr	Angstroms	mol/cm^2	$\mu C/cm^2$
5.2	3.52861	3.08E-09	594.34839
8.2	3.53281	3.07E-09	592.93604
9.9	3.53519	3.07E-09	592.13794
11.7	3.53771	3.06E-09	591.29465
14.9	3.54219	3.06E-09	589.79991
16.6	3.54457	3.05E-09	589.00814
23.1	3.55367	3.04E-09	585.99541
24.1	3.55507	3.03E-09	585.53397

Table 4.1. Calculated parameters as a function of Cr composition.

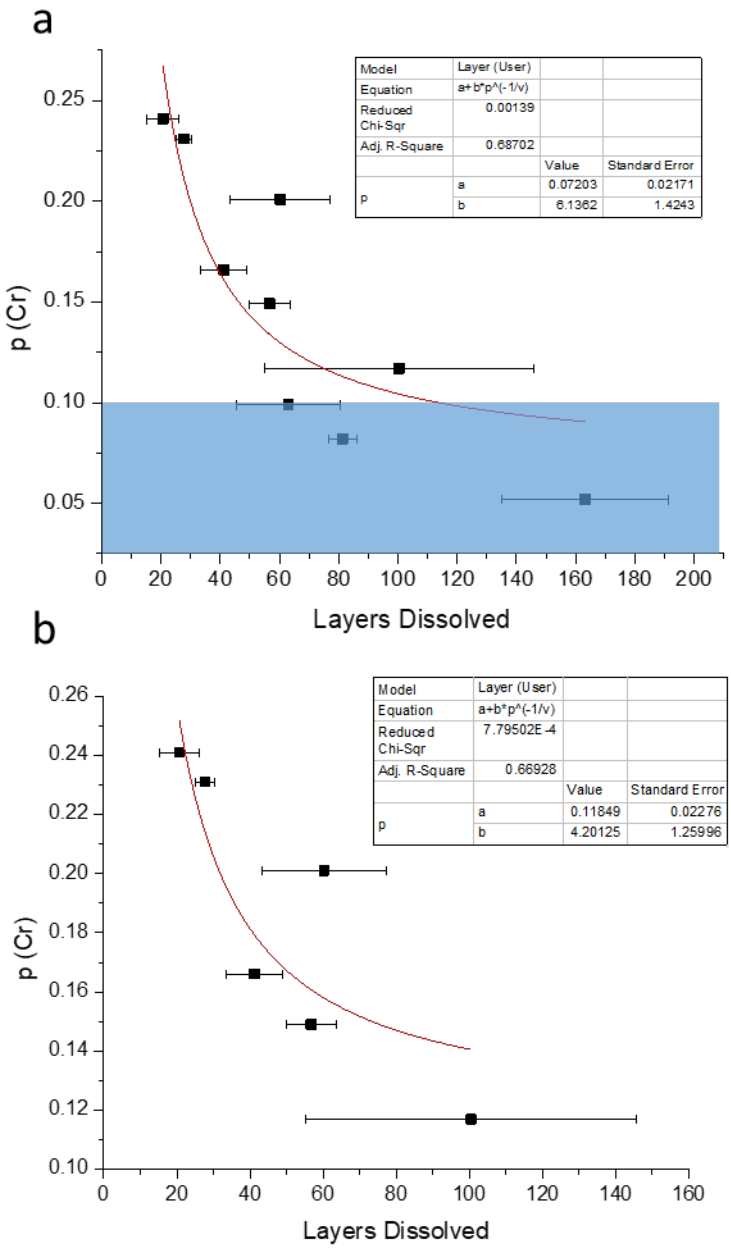

Figure 4.11. Preliminary results showing number of monolayers dissolved as a function of at.% Cr composition. A reasonable fit to the equation $p_c(h) = p_c^{3D} + c\, h^{-1/\nu^{3D}}$ has been achieved using $\nu^{3D} = 0.878$. A fit was applied to data from (a) all alloy compositions where $c = 6.14$ and $p_c^{3D} = 0.072$ and (b) compositions excluding the blue marked region in (a) where $c = 4.20$ and $p_c^{3D} = 0.118$.

To finalize the comparison, the number of dissolved layers as a function of Cr composition was fit to the percolation threshold equation (4.1.) previously described by Sotta and Long, as shown in Figure 4.11. We fit c and p_c^{3D} using the known values of h (calculated average number of monolayers), v^{3D} (equal to 0.878), and p_c (Cr composition) to the full data set (Figure 4.11.a) and also to a smaller data set including only alloy compositions above 10 at.% Cr (Figure 4.11.b) since we believe passivation behavior at lower concentrations to behave independently of percolation theory. We obtain fitted values of $c = 6.14$ and $p_c^{3D} = 0.072$ using all data points and $c = 4.20$ and $p_c^{3D} = 0.118$ using only compositions of interest, both of which are a reasonably good fit to the expected p_c^{3D} theoretical value of 0.137. A plausible reason for this discrepancy is due to the fact that experimental measurements rely on the average number of monolayers dissolved whereas the theoretical value relies on highest number of monolayers dissolved. Additionally, kinetics have not been considered in this interpretation of percolation theory. The contribution of surface mobilities of Cr atoms during the period of active dissolution is unknown

4.5 Summary and Conclusion

Using electrochemical studies, passivation behavior of single-phase binary Ni-Cr alloys has been examined. Polarization curves have emphasized the dependence of passivity on the Cr composition through shifts in the critical current density and passivation potential. Other corrosion-related electrochemical parameters, namely the corrosion potential and

transpassive potential, were weakly dependent on Cr composition. These studies have been found to be in good agreement with other similar electrochemical studies reported in the literature. Potential pulse studies lend support towards the use of percolation theory as an explanation for the 12 at.% Cr requirement to achieve passivity in Ni-Cr alloys. The monolayer dissolution data fits well to the theoretical model by Sotta and Long, and the fitted p_c^{3D} value of 0.118 is in good agreement with the theoretical value of 0.137.

From these results, we would expect passivity in single-phase binary alloys to be achievable with the addition of a more "noble element" in concentrations exceeding the 3D percolation threshold in solid solution with a more active component. The more noble element in must be either corrosion resistant and free of an atmospherically-produced oxide (i.e. Au) or form a strong passive film in atmospheric conditions. As previously mentioned, good passive films are thin, stable, self-healing, and corrosion resistant. As shown in the case of chromium, although the elemental metal is more electrochemically active than iron and nickel, chromium oxide is a strong passive film that is significantly more noble in comparison with iron and nickel. The 3D percolation threshold will depend on the crystal structure and degree of contributing nearest neighbors. Although these conditions have yet to be explored in multiple alloy systems, results obtained from the Ni-Cr system have led us to suspect that they may play a large contributing role in the passivation mechanism.

5 Conclusions and Future Work

The focus of this thesis has been on the study of corrosion mechanisms in single-phase binary alloys to elucidate some of the topical issues regarding passivation mechanisms in hopes of developing new “stainless-like” materials. In Chapter 3, we examine Mg-xAl alloys, a highly reactive system with great industrial appeal as a lightweight alloy. Compositional changes are observed at the surface as a direct result of the corrosion process, primarily in the form of Al enrichment, using polarization testing and “accelerated” free corrosion. During “accelerated” aqueous corrosion, enrichment was observed in the form of Al-rich platelet morphology evolution. In ionic liquid studies, both Al-rich platelets and Al nanowire morphologies were observed.

We attribute these morphologies to the preferential dissolution of Mg and surface mobility of Al. In the α-matrix composed of Al in solid solution with Mg, Mg is characterized as the more reactive component and Al the more “noble” component. When placed in a corrosive environment, microgalvanic corrosion ensues, where Mg preferentially dissolves from sites with fewer nearest neighbors (i.e. step and kink sites). Al diffuses along the step edges, eventually forming Al-rich structures. The mechanism governing structure type has yet to be determined and will require additional study.

In both “accelerated” corrosion and ionic liquid studies, hydroxide layer buildup is reduced. “Accelerated” corrosion studies rely on the use of a rotating disk electrode, which allows for continuous laminar flow across the sample surface, minimizing the

diffusion boundary layer and increasing the concentration gradient. Ionic liquid studies at elevated temperature in argon environment also work to prevent the hydrogen evolution mechanism by limiting water exposure at the sample surface. By limiting pH increases at the surface, Al remains stable, allowing for subsequent Al enrichment. The Al nanowires formed in ionic liquid on αMg-5 at.% Al are reminiscent of metallic nanowires formed by spontaneous electrodeposition at surface step edges described by Robert Dryfe et. al. [93]. Aside from these general remarks, the exact mechanism behind the observed Al-rich structures remains unanswered. In an effort to gain a more complete understanding, kinetic Monte Carlo (KMC) simulations will be performed using the experimentally derived first-rate kinetic parameters.

Chapter 4 continues to explore passivity in single-phase binary alloys, this time in the "ideal" Ni-Cr system. Ni-Cr displays "stainless-like" passivity in most dilute, aerated solutions with additions of 12-13 at.% Cr. In the Ni-Cr system, Ni serves as the active component and Cr the more "noble" component. By electrochemically evaluating the passivation behavior of Ni-xCr alloys as a function of composition, the passivation potential, critical current density, and passivation current density were all found to decrease with increasing Cr composition. Potential pulse studies were used to better evaluate the time-dependent passivation behavior, allowing for more accurate passivation current density and monolayer dissolution measurements. The measured number of average monolayers dissolved during the active dissolution and primary passivation regimes was fit to the theoretical model by Sotta and Long and found to be in good

agreement. To determine the accuracy of these preliminary results, KMC simulations will be used to observe the theoretical corrosion behavior of these alloys for comparison with experimental results and the theoretical model by Sotta and Long. These results can also be compared with the Fe-Cr system, another “stainless-like” system that has been well studied.

From our results, we believe passivity to be connected with percolation theory. Enough “noble” atoms must be present in the lattice to form the infinite cluster, allowing for passive film formation. When the “noble” element composition is too low, the alloy is unable to passivate. The required composition is determined by the percolation threshold, which is affected by crystal structure, passive film composition, and lattice spacing. In the case of Mg-Al alloys, the site percolation threshold is near 0.2, meaning that below 20 at.% Al in solid solution, passivity is not observed. We know from the Mg-Al phase diagram that these conditions are not thermodynamically favorable. Thus, in order to achieve “stainless-like” behavior in this system, some additional component(s) would be needed to stabilize the required Al composition in the α-matrix. Thermodynamic calculation would be required to determine what alloying agents may be suitable for this.

REFERENCES

[1] Huang, P.; Latham, J.-A.; MacFarlane, D. R.; Howlett, P. C.; Forsyth, M. A Review of Ionic Liquid Surface Film Formation on Mg and Its Alloys for Improved Corrosion Performance. *Electrochim. Acta* **2013**, *110*, 501–510.

[2] Wu, G.; Ibrahim, J. M.; Chu, P. K. Surface Design of Biodegradable Magnesium Alloys - A Review. *Surf. Coatings Technol.* **2013**, *233*, 2–12.

[3] Ali, Y.; Qiu, D.; Jiang, B.; Pan, F.; Zhang, M. X. Current Research Progress in Grain Refinement of Cast Magnesium Alloys: A Review Article. *J. Alloys Compd.* **2015**, *619*, 639–651.

[4] Hornberger, H.; Virtanen, S.; Boccaccini, A. R. Biomedical Coatings on Magnesium Alloys - A Review. *Acta Biomater.* **2012**, *8* (7), 2442–2455.

[5] Song, G.; Atrens, A. Recent Insights into the Mechanism of Magnesium Corrosion and Research Suggestions. *Adv. Eng. Mater.* **2007**, *9* (3), 177–183.

[6] Ding, Y.; Wen, C.; Hodgson, P.; Li, Y. Effects of Alloying Elements on the Corrosion Behavior and Biocompatibility of Biodegradable Magnesium Alloys: A Review. *J. Mater. Chem. B* **2014**, *2* (14), 1912–1933.

[7] Makar, G. L.; Kruger, J. Corrosion Studies of Rapidly Solidified Magnesium Alloys. *J. Electrochem. Soc.* **1990**, *137* (2), 414–421.

[8] *ASM Speciality Handbook: Magnesium and Magnesium Alloys*; Avedesian, M. M., Baker, H., Eds.; ASM International: Materials Park, 1999.

[9] Pourbaix, M. *Atlas of Electrochemical Equilibria in Aqueous Solutions*, 2nd ed.; National Association of Corrosion Engineers: Houston, 1974.

[10] Nanjo, H.; Laycock, N. J.; Deng, H.; Ishikawa, I.; Sanada, N. Atomic-Scale Flattening of Ni-Cr Alloy Surfaces by Electrochemical Passivation Treatments. *Curr. Appl. Phys.* **2004**, *4* (2–4), 156–159.

[11] Myers, J. R.; Beck, F. H.; Fontana, M. G. Anodic Polarization Behavior of Nickel-Chromium Alloys in Sulfuric Acid Solutions. *Corrosion* **1965**, *21* (9), 277–287.

[12] Bond, a. P.; Uhlig, H. H. Corrosion Behavior and Passivity of Nickel-Chromium and Cobalt-Chromium Alloys. *J. Electrochem. Soc.* **1960**, *107* (6), 488.

[13] Davis, J. R. *Concise Metals Engineering Data Book*; ASM International, 1997.

[14] Jones, D. A. *Principles and Prevention of Corrosion*, 2nd ed.; Prentice Hall: Upper Saddle River, 1996.

[15] Hiromoto, S. Self-Healing Property of Hydroxyapatite and Octacalcium Phosphate Coatings on Pure Magnesium and Magnesium Alloy. *Corros. Sci.* **2015**, *100*, 284–294.

[16] Bhargava, G.; Allen, F. Self-Healing, Chromate-Free Conversion Coating for Magnesium Alloys. *Met. Finish.* **2012**, *110* (4), 32–38.

[17] Gu, C. D.; Yan, W.; Zhang, J. L.; Tu, J. P. Corrosion Resistance of AZ31B Magnesium Alloy with a Conversion Coating Produced from a Choline Chloride—Urea Based Deep Eutectic Solvent. *Corros. Sci.* **2016**, *106*, 108–116.

[18] Howlett, P. C.; Gramet, S.; Lin, J.; Efthimiadis, J.; Chen, X. B.; Birbilis, N.; Forsyth, M. Conversion Coatings of Mg-Alloy AZ91D Using Trihexyl(Tetradecyl) Phosphonium Bis(Trifluoromethanesulfonyl)Amide Ionic Liquid. *Sci. China Chem.* **2012**, *55* (8), 1598–1607.

[19] Bland, L. G.; Birbilis, N.; Scully, J. R. Exploring the Effects of Intermetallic Particle Size and Spacing on the Corrosion of Mg-Al Alloys Using Model Electrodes. *J. Electrochem. Soc.* **2016**, *163* (14), C895–C906.

[20] Mathieu, S.; Rapin, C.; Steinmetz, J.; Steinmetz, P. A Corrosion Study of the Main Constituent Phases of AZ91 Magnesium Alloys. *Corros. Sci.* **2003**, *45*, 2741–2755.

[21] O. Lunder, J.E. Lein, T.K.R. Aune, K. N. The Role of the Mg17Al12 Phase in the Corrosion of Mg Alloy AZ91. *Corrosion* **1989**, *45* (9), 741–748.

[22] O. Lunder, T.K.R. Aune, K. N. Effect of Mn Additions on the Corrosion Behaviour of Mould-Cast Magnesium ASTM AZ91. *Corrosion* **1987**, *43* (5), 291–295.

[23] Aung, N. N.; Zhou, W. Effect of Grain Size and Twins on Corrosion Behaviour of AZ31B Magnesium Alloy. *Corros. Sci.* **2010**, *52* (2), 589–594.

[24] Feng, H.; Liu, S.; Du, Y.; Lei, T.; Zeng, R.; Yuan, T. Effect of the Second Phases on Corrosion Behavior of the Mg-Al-Zn Alloys. *J. Alloys Compd.* **2017**, *695*, 2330–2338.

[25] Xu, W.; Birbilis, N.; Sha, G.; Wang, Y.; Daniels, J. E.; Xiao, Y.; Ferry, M. A High-Specific-Strength and Corrosion-Resistant Magnesium Alloy. *Nat. Mater.* **2015**, *14* (12), 1229–1236.

[26] Hou, L.; Raveggi, M.; Chen, X.-B.; Xu, W.; Laws, K. J.; Wei, Y.; Ferry, M.; Birbilis, N. Investigating the Passivity and Dissolution of a Corrosion Resistant Mg-33at.%Li Alloy in Aqueous Chloride Using Online ICP-MS. *J. Electrochem. Soc.* **2016**, *163* (6), C324–C329.

[27] Makar, G. L.; Kruger, J. Corrosion Studies of Rapidly Solidified Magnesium Alloys. *J. Electrochem. Soc.* **1990**, *137* (2), 414–421.

[28] Singh, I. B.; Singh, M.; Das, S. A Comparative Corrosion Behavior of Mg, AZ31 and AZ91 Alloys in 3.5% NaCl Solution. *J. Magnes. Alloy.* **2015**, *3* (2), 142–148.

[29] Kulekci, M. K. Magnesium and Its Alloys Applications in Automotive Industry.

Int. J. Adv. Manuf. Technol. **2008**, *39* (9–10), 851–865.

[30] Zander, D.; Schnatterer, C. The Influence of Manufacturing Processes on the Microstructure and Corrosion of the AZ91D Magnesium Alloy Evaluated Using a Computational Image Analysis. *Corros. Sci.* **2015**, *98*, 291–303.

[31] Parthiban, G. T.; Palaniswamy, N.; Sivan, V. Effect of Manganese Addition on Anode Characteristics of Electrolytic Magnesium. *Anti-Corrosion Methods Mater.* **2009**, *56* (2), 79–83.

[32] Caceres, C. H.; Blake, A. The Strength of Concentrated Mg – Zn Solid Solutions. *Phys. Status Solidi* **2002**, *194* (1), 147–158.

[33] Blake, A. H.; Caceres, C. H. Solid-Solution Hardening and Softening in Mg-Zn Alloys. *Mater. Sci. Eng. A* **2008**, No. 483–484, 161–163.

[34] Chun, J. S.; Byrne, J. G. Precipitate Strengthening Mechanisms in Magnesium Zinc Alloy Single Crystals. *J. Mater. Sci.* **1969**, *4*, 861–872.

[35] Okamoto, H. Supplemental Literature Review of Binary Phase Diagrams: Al-Mg, Bi-Sr, Ce-Cu, Co-Nd, Cu-Nd, Dy-Pb, Fe-Nb, Nd-Pb, Pb-Pr, Pb-Tb, Pd-Sb, and Si-W. *J. Phase Equilibria Diffus.* **2015**, *36* (2), 183–195.

[36] Song, G.; Atrens, A. Corrosion Mechanisms of Magnesium Alloys. *Adv. Eng. Mater.* **1999**, *1* (1), 11–33.

[37] Huber, K. Anodic Formation of Coatings on Magnesium, Zinc, and Cadmium. *J. Electrochem. Soc.* **1953**, *100*, 376–382.

[38] Fruhwirth, O.; Herzog, G. W.; Hollerer, I.; Rachetti, A. Dissolution and Hydration Kinetics of MgO. *Surf. Technol.* **1985**, *24* (3), 301–317.

[39] Yamaguchi, S. Protective Films on Magnesium Observed by Electron Diffraction and Microscopy [4]. *J. Appl. Phys.* **1954**, *25* (11), 1437–1438.

[40] Hanawalt, J. D.; Nelson, C. E.; Peloubet, J. A. Transactions of the American Institute of Mining and Metallurgical Engineers. *Trans. AIME* **1942**, *147*, 279–299.

[41] Kruger, J.; Long, G. G.; Zhang, Z.; Tanaka, D. K. The Use of X-Ray Adsorption Spectroscopic Techniques to Study the Influence of Alloying Elements on Passive Films. *Corros. Sci.* **1990**, *31*, 111–120.

[42] Unocic, K. A.; Elsentriecy, H. H.; Brady, M. P.; Meyer, H. M.; Song, G. L.; Fayek, M.; Meisner, R. A.; Davis, B. Transmission Electron Microscopy Study of Aqueous Film Formation and Evolution on Magnesium Alloys. *J. Electrochem. Soc.* **2014**, *161* (6), C302–C311.

[43] Eisenberg, M.; Tobias, C. W.; Wilke, C. R. Ionic Mass Transfer and Concentration Polarization at Rotating Electrodes. *J. Electrochem. Soc.* **1954**, *101* (6), 306–320.

[44] Pang, J.; Ritchie, I. M. Mass Transfer At the Surface Cylinder. **1981**, *26* (9), 1345–1350.

[45] Bender, S.; Goellner, J.; Heyn, A.; Boese, E. Corrosion and Corrosion Testing of Magnesium Alloys. *Mater. Corros.* **2007**, *58* (12), 977–982.

[46] Marco, I.; Van der Biest, O. Polarization Measurements from a Rotating Disc Electrode for Characterization of Magnesium Corrosion. *Corros. Sci.* **2016**, *102*, 384–393.

[47] Howlett, P. C.; MacFarlane, D. R.; Hollenkamp, A. F. High Lithium Metal Cycling Efficiency in a Room-Temperature Ionic Liquid. *Electrochem. Solid-State Lett.* **2004**, *7* (5), A97.

[48] Howlett, P. C.; Brack, N.; Hollenkamp, A. F.; Forsyth, M.; MacFarlane, D. R. Characterization of the Lithium Surface in N-Methyl-N-Alkylpyrrolidinium Bis(Trifluoromethanesulfonyl)Amide Room-Temperature Ionic Liquid Electrolytes. *J. Electrochem. Soc.* **2006**, *153* (3), A595.

[49] Forsyth, M.; Neil, W. C.; Howlett, P. C.; MacFarlane, D. R.; Hinton, B. R. W.; Rocher, N.; Kemp, T. F.; Smith, M. E. New Insights into the Fundamental Chemical Nature of Ionic Liquid Film Formation on Magnesium Alloy Surfaces. *ACS Appl. Mater. Interfaces* **2009**, *1* (5), 1045–1052.

[50] Latham, J.-A.; Howlett, P. C.; MacFarlane, D. R.; Forsyth, M. Passive Film Formation in Dilute Ionic Liquid Solutions on Magnesium Alloy AZ31. *Electrochem. commun.* **2012**, *19*, 90–92.

[51] Birbilis, N.; Howlett, P. C.; MacFarlane, D. R.; Forsyth, M. Exploring Corrosion Protection of Mg via Ionic Liquid Pretreatment. *Surf. Coatings Technol.* **2007**, *201* (8), 4496–4504.

[52] Howlett, P. C.; Zhang, S.; MacFarlane, D. R.; Forsyth, M. An Investigation of a Phosphinate-Based Ionic Liquid for Corrosion Protection of Magnesium Alloy AZ31. *Aust. J. Chem.* **2007**, *60* (1), 43.

[53] Macfarlane, D. R.; Forsyth, M.; Howlett, P. C.; Jennifer, M.; Sun, J.; Annat, G.; Neil, W.; Izgorodina, E. I.; Pringle, J. M. Ionic Liquids in Electrochemical Devices and Processes : Managing Interfacial Electrochemistry Ionic Liquids in Electrochemical Devices and Processes : Managing Interfacial Electrochemistry. **2007**, *40* (11), 1165–1173.

[54] Sun, J.; Howlett, P. C.; MacFarlane, D. R.; Lin, J.; Forsyth, M. Synthesis and Physical Property Characterisation of Phosphonium Ionic Liquids Based on P(O)2(OR)2- and P(O)2(R)2- Anions with Potential Application for Corrosion Mitigation of Magnesium Alloys. *Electrochim. Acta* **2008**, *54* (2), 254–260.

[55] Efthimiadis, J.; Neil, W. C.; Bunter, A.; Howlett, P. C.; Hinton, B. R. W.; MacFarlane, D. R.; Forsyth, M. Potentiostatic Control of Ionic Liquid Surface

Film Formation on ZE41 Magnesium Alloy. *ACS Appl. Mater. Interfaces* **2010**, *2* (5), 1317–1323.

[56] Howlett, P. C.; Khoo, T.; Mooketsi, G.; Efthimiadis, J.; MacFarlane, D. R.; Forsyth, M. The Effect of Potential Bias on the Formation of Ionic Liquid Generated Surface Films on Mg Alloys. *Electrochim. Acta* **2010**, *55* (7), 2377–2383.

[57] Latham, J. A.; Howlett, P. C.; MacFarlane, D. R.; Forsyth, M. Electrochemical Reactivity of Trihexyl(Tetradecyl)Phosphonium Bis(2,4,4-Trimethylpentyl)Phosphinate Ionic Liquid on Glassy Carbon and AZ31 Magnesium Alloy. *Electrochim. Acta* **2011**, *56* (15), 5328–5334.

[58] Chen, Q.; Sieradzki, K. Spontaneous Evolution of Bicontinuous Nanostructures in Dealloyed Li-Based Systems. *Nat. Mater.* **2013**, *12* (12), 1102–1106.

[59] Voort, G. Vander. Metallography of Magnesium and Its Alloys. *Buehler Tech Notes* **2015**, *4* (2), 1–5.

[60] Chen, Q.; Sieradzki, K. Mechanisms and Morphology Evolution in Dealloying. *J. Electrochem. Soc.* **2013**, *160* (6), C226–C231.

[61] Ambat, R.; Aung, N. N. N.; Zhou, W. Evaluation of Microstructural Effects on Corrosion Behaviour of AZ91D Magnesium Alloy. *Corros. Sci.* **2000**, *42* (8), 1433–1455.

[62] Buzza, D. W. Growth of Corrosion Pits on Pure Aluminum in 1M NaCl. *J. Electrochem. Soc.* **1995**, *142* (4), 1104.

[63] Fajardo, S.; Frankel, G. S. S. Effect of Impurities on the Enhanced Catalytic Activity for Hydrogen Evolution in High Purity Magnesium. *Electrochim. Acta* **2015**, *165*, 255–267.

[64] Muller, I. L.; Galvele, J. R. Pitting Potential of High Purity Binary Aluminium Alloys—II. AlMg and AlZn Alloys. *Corros. Sci.* **1977**, *17* (12), 995–1007.

[65] McCall, C. R.; Hill, M. A.; Lillard, R. S. Crystallographic Pitting in Magnesium Single Crystals. *Corros. Eng. Sci. Technol.* **2005**, *40* (4), 337–343.

[66] Lafront, A. M.; Zhang, W.; Jin, S.; Tremblay, R.; Dubé, D.; Ghali, E. Pitting Corrosion of AZ91D and AJ62x Magnesium Alloys in Alkaline Chloride Medium Using Electrochemical Techniques. *Electrochim. Acta* **2005**, *51* (3), 489–501.

[67] Frankel, G. S. On the Pitting Resistance of Sputter-Deposited Aluminum Alloys. *J. Electrochem. Soc.* **1993**, *140* (8), 2192.

[68] Pyun, S. Il; Na, K. H.; Park, J. J. Morphological Studies of the Mechanism of Pit Growth of Pure Aluminum in Sulfate Ion- or Nitrate Ion-Containing 0.1 M NaCl Solutions. *J. Solid State Electrochem.* **2001**, *5* (7–8), 473–478.

[69] Bard, A. J.; Faulkner, L. R. *Electrochemical Methods: Fundamentals and Applications*, 2nd ed.; John Wiley & Sons, Inc., 2001.

[70] Wenzel, R. N. Resistance of Solid Surfaces to Wetting by Water. *Ind. Eng. Chem.* **1936**, *28* (8), 988–994.

[71] Culberson, C. H.; Pytkowicz, R. M. Ionization of Water in Seawater. *Mar. Chem.* **1973**, *1*, 309–316.

[72] Millero, F. J.; Sohn, M. L. *Chemical Oceanography*; CRC Press: Boca Raton, 1992.

[73] Singh, R. *Membrane Technology and Engineering for Water Purification*, 2nd ed.; Elsevier: Amsterdam, 2015.

[74] Shante, V. K. S.; Kirkpatrick, S. An Introduction to Percolation Theory. *Adv. Phys.* **1971**, *20* (85), 325–357.

[75] Totemeier, W. F. G. and T. C. *Smithells Metals Reference Book*, 8th ed.; Elsevier, 2004.

[76] Greene, M. G. F. and N. D. *Corrosion Engineering*; McGraw-Hill, 1967.

[77] Luo, L.; Zou, L.; Schreiber, D. K.; Baer, D. R.; Bruemmer, S. M.; Zhou, G.; Wang, C. Scripta Materialia In-Situ Transmission Electron Microscopy Study of Surface Oxidation for Ni – 10Cr and Ni – 20Cr Alloys. *Smm* **2016**, *114*, 129–132.

[78] Jeng, S. P.; Holloway, P. H.; Batich, C. D. Surface Passivation of Ni/Cr Alloy at Room Temperature. *Surf. Sci.* **1990**, *227* (3), 278–290.

[79] Frankenthal, R. P. On the Passivity of Iron-Chromium Alloys I. Reversible Primary Passivation and Secondary Film Formation. *J. Electrochem. Soc.* **1967**, *114* (6), 542–547.

[80] Frankenthal, R. P. On the Passivity of Iron-Chromium Alloys II. The Activation Potential. *J. Electrochem. Soc.* **1969**, *116* (5), 580–585.

[81] Frankenthal, R. P. On the Passivity of Iron-Chromium Alloys III. Effect of Potential. *J. Electrochem. Soc.* **1969**, *116* (12), 1646–1651.

[82] Ryan, M. P.; Newman, R. C.; Thompson, G. E. A Scanning Tunnelling Microscopy Study of Structure and Structural Relaxation in Passive Oxide Films on Fe-Cr Alloys. *Philos. Mag. Part B* **1994**, *70* (2), 241–251.

[83] Kirchheim, R.; Heine, B.; Fischmeister, H.; Hofmann, S.; Knote, H.; Stolz, U. The Passivity of Iron-Chromium Alloys. *Corros. Sci.* **1989**, *29* (7), 899–917.

[84] Economy, G.; Rudolph Speiser; BECK, F. H.; FONTANA, M. G. Anodic Polarization Behavior of Nickel-Chromium Alloys in Sulfuric Acid Solutions. *J. Electrochem. Soc.* **1961**, *108* (4), 337–343.

[85] Sieradzki, K.; Newman, R. C. Percolation Model for Passivation in Stainless Steels. *J. Electrochem. Soc.* **1986**, *133* (9), 1979–1980.

[86] Qian, S. Validation of a Percolation Model for Passivation of Fe-Cr Alloys: Two-Dimensional Computer Simulations. *J. Electrochem. Soc.* **1990**, *137* (2), 435.

[87] Qian, S.; Newman, R. C.; Cottis, R. A.; Sieradzki, K. Computer Simulation of Alloy Passivation and Activation. *Corros. Sci.* **1990**, *31* (C), 621–626.

[88] Newman, R. C.; Foong Tuck Meng; Sieradzki, K. Validation of a Percolation Model for Passivation of FeCr Alloys: I Current Efficiency in the Incompletely Passivated State. *Corros. Sci.* **1988**, *28* (5), 523–527.

[89] Sotta, P.; Long, D. The Crossover from 2D to 3D Percolation: Theory and Numerical Simulations. *Eur. Phys. J. E* **2003**, *11* (4), 375–388.

[90] Beck, T. R. Formation of Salt Films during Passivation of Iron. *J. Electrochem. Soc.* **1982**, *129* (11), 2412.

[91] Banaś, J.; Mazurkiewicz, B.; Stypuła, B. Passivity of Metals in Concentrated and Anhydrous Solutions of Sulphuric Acid. *Electrochim. Acta* **1992**, *37* (6), 1069–1073.

[92] Wu, C.; Lee, B. J.; Su, X. Modified Embedded-Atom Interatomic Potential for Fe-Ni, Cr-Ni and Fe-Cr-Ni Systems. *Calphad Comput. Coupling Phase Diagrams Thermochem.* **2017**, *57* (November 2016), 98–106.

[93] Dryfe, R. A. W.; Walter, E. C.; Penner, R. M. Electrodeposition of Metal Nanostructures by Galvanic Displacement Powered with Insoluble Crystals of a Ferrocene Derivative. *ChemPhysChem* **2004**, *5* (12), 1879–1884.